Journal of Translational Medicine

RESEARCH

Open Access

AC129507.1 is a ferroptosis-related target identified by a novel mitochondria-related lncRNA signature that is involved in the tumor immune microenvironment in gastric cancer

Shanshan Yu[1†], Jinxiao Liang[1†], Lixiao Liu[2†], Ming Chen[3], Cheng Chen[1] and Donghui Zhou[1*]

Abstract

Background Gastric cancer (GC) is one of the most common malignancies. Previous studies have shown that mitochondrial metabolism is associated with malignancies. However, relevant research on mitochondria-related lncRNAs in GC is lacking.

Methods We integrated the corresponding information of patients with GC from The Cancer Genome Atlas (TCGA) database. Mitochondria-related lncRNAs were selected based on differential expression and a correlation analysis to construct a prognostic model. The mutation data were analyzed to distinguish differences in the tumor mutation burden (TMB). Single-sample gene set enrichment analysis (ssGSEA) was performed to evaluate immunological differences. A series of cell-based experiments were adopted to evaluate the biological behavior of GC.

Results A total of 1571 mitochondria-related lncRNAs were identified. A prognostic signature incorporating nine lncRNAs was built based on 293 suitable GC cases and could predict patient prognosis. The TMB and ssGSEA indicated that the low-risk group displayed increased immune function. The enrichment analysis indicated that the differentially expressed genes were enriched in metabolic functions. AC129507.1 was significantly upregulated in GC cells and associated with a poor prognosis, and its knockdown inhibited the proliferation and migration of GC cells. Mechanistically, silencing AC129507.1 led to abnormal glycolipid metabolism and oxidative stress, thus inducing ferroptosis.

Conclusions Our nine-lncRNA risk signature could powerfully predict patient prognosis. AC129507.1 promoted the malignant phenotypes of GC cells. AC129507.1 could play a nonnegligible role in GC by promoting the formation of a immunosuppressive tumor microenvironment by inhibiting the initiation of ferroptosis, which needs to be further explored.

Keywords Gastric cancer, Mitochondria, Long noncoding RNA, Metabolism, Ferroptosis, Tumor microenvironment

†Shanshan Yu, Jinxiao Liang and Lixiao Liu contributed equally to this work.

*Correspondence:
Donghui Zhou
donghui.zhou@zju.edu.cn
Full list of author information is available at the end of the article

Introduction

According to the latest report on global cancer data, China is the country with the greatest number of new cancer cases and cancer-related deaths, with 480,000 new cases of gastric cancer, ranking third among new cancer cases in China [1]. Although the incidence rate and mortality of GC patients have decreased to a certain extent with the continuous improvements in diagnosis and treatment technology and attention given to early screening, the prognosis of patients with advanced GC has not significantly improved, and their five-year survival rate is still low [2]. Gastric cancer is a malignant tumor with high heterogeneity in histopathology, molecule levels, metabolic characteristics and immune cell infiltration, which also leads to complex clinical treatments and a poor prognosis [3, 4]. Therefore, actively exploring potential targets and mechanisms from multiple levels and perspectives is particularly important.

Malignant tumors are abnormal new tissues with high metabolism and high energy consumption, which means that mitochondria, known as energy factories, are inextricably linked to the occurrence and development of malignant tumors [5–7]. Under normal circumstances, mitochondria are responsible for production capacity via the citric acid (TCA) cycle and play important roles in maintaining the homeostasis of the internal environment, biosynthesis, metabolism and other important physiological processes [8, 9]. However, when abnormal gene mutations accumulate in the body to a certain extent, they can also lead to changes in mitochondrial functional metabolism, drive metabolic reprogramming, and induce glycolysis, thus promoting tumor growth [7, 10, 11]. Rabe et al. found that succinic acid receptor 1 (sunr1), a key protein in the TCA cycle, can promote the growth of GC cells by limiting TCA cycle flux, mitochondrial respiration and the production of ROS and that the knockdown of this gene can sensitize gastric cancer cells to chemotherapy [12]. In addition, the metabolic transformation caused by mitochondrial disorders can rearrange the metabolites of the tumor microenvironment, especially the accumulation of lactic acid, while cancer cells further use lactic acid to promote their growth and mitochondrial metabolism and shape an immune microenvironment suitable for tumor growth through immunomodulatory effects [13–15]. Therefore, analyzing mitochondria-related genes from multiple metabolic and immune perspectives and exploring their functions in GC may provide new ideas and strategies for the current treatment of GC.

The rapid development of genomic technology has deepened our understanding of the human genome. The noncoding sequences that account for 98.5% of the human genome have attracted much attention, and the discovery of tens of thousands of long noncoding RNAs (lncRNAs) has completely changed the way researchers think about the occurrence and development of diseases [16, 17]. Long noncoding RNAs are considered the transcriptional products of noncoding genes, which are longer than 200 nucleotides (nt) and usually do not express protein products; however, recent studies suggest that some lncRNAs can encode small peptides or small proteins [18, 19]. Increasing evidence shows that lncRNAs play crucial roles in a variety of disease processes and physiological states, especially tumorigenesis and metastasis [20–22]. For example, the lncRNA ELF3-AS1 localized in the nucleus can not only negatively regulate GC cell cycle progression by inhibiting the G1/S transition and histone synthesis but also inhibit GC metastasis by inhibiting the SNAI2 signaling pathway [23]. Moreover, the upregulated expression of lncRNA-SNHG16 in GC tissues is closely related to the 5-Fu resistance of GC, and its downregulation can regulate the level of glucose metabolism in GC through the miR-506-3p-PTBP1 axis to attenuate the 5-Fu resistance of GC, providing a promising method for the treatment of chemotherapy resistance [24]. In addition, researchers have reported that a significantly downregulated lncRNA in GC functions as a tumor suppressor, affecting the proliferation and invasion of GC by regulating the expression of a gene subset in the p53 pathway at the transcriptional level through the BRD7/TP53 signaling pathway, which is related to a poor prognosis [25]. Although an increasing number of studies have been conducted on the roles of various novel lncRNAs in GC, the roles of mitochondria-related lncRNAs in GC remain to be further explored. Therefore, the exploration of mitochondria-related lncRNA biomarkers in GC is important for clinical diagnosis and treatment.

In our study, we constructed and validated a novel prognostic model for GC based on nine prognostic mitochondria-related lncRNAs. Our model showed satisfactory performance in predicting the prognosis of GC patients and was considered an independent risk predictive factor. In addition, our risk score was closely associated with a high tumor mutation burden (TMB) and cellular infiltration and turbulence in the immune microenvironment. These corresponding differentially expressed genes that were significantly correlated with lncRNAs were enriched in some pathways related to lipid metabolism, glucose metabolism, and oxidative stress. We identified and selected AC129507.1, a lncRNA highly expressed in GC cell lines, for further in vitro studies to confirm the importance of these nine prognostic lncRNAs. The downregulation of AC129507.1 not only significantly inhibited the proliferation and invasion of GC cells in vitro but also suppressed the growth of transplanted tumors in vivo. Furthermore, the downregulation of

AC129507.1 could contribute to the initiation of ferroptosis, which affected the efficacy of GC immunotherapy by regulating the levels of lipid and glucose metabolism.

Methods

Data collection and processing

The transcriptional data and relevant clinicopathological information of patients with GC, including 343 tumor samples and 30 normal samples, were downloaded from TCGA database. The clinicopathological information included the survival time, survival state, age, sex, grade, stage, T stage, N stage and M stage, and patients with survival times less than 90 days were discarded. The entire cohort, which included 293 GC patients, was randomly divided at a ratio of 1:1 into a training cohort (n = 147) and a validation cohort (n = 146). The training cohort was adopted to construct the risk model, and the testing cohort and entire cohort were used to verify the risk model. Additionally, 1136 mitochondria-related genes were obtained from previous research (Supplementary Table S1), and their expression levels were extracted from TCGA GC dataset [26].

Screening of mitochondria-related lncRNAs

After the transcriptional data and expression files from TCGA database were downloaded and the Ensemble IDs of the genes were recognized by running the corresponding script file, all the lncRNAs were extracted. We then conducted a differential expression analysis between 343 tumor samples and 30 normal samples to identify differentially expressed mitochondria-related genes (DEMGs). Based on the data and information obtained above, we conducted a correlation analysis between DEMGs and lncRNAs, with a correlation coefficient > 0.5 and $P < 0.001$ as the boundaries, and the results were visualized in a Sankey diagram.

Construction and validation of the prognostic model based on mitochondria-related lncRNAs

A univariate Cox regression analysis was conducted to screen for prognostic mitochondria-related lncRNAs with a threshold of $p < 0.05$. Based on the results of the univariate Cox regression analysis, LASSO regression was performed to reduce the dimensions of high-dimensional data by penalty rules, preserving potential predictive variables with nonzero coefficients to avoid overfitting the model [27]. We then employed a multivariate Cox regression analysis to identify the specific mitochondria-related lncRNAs included in the final prognostic model. According to the results of the multivariate Cox regression analysis, the risk score of each GC patient was calculated. The risk score formula was as follows:$\text{risk score} = \sum_{i=1}^{n}(\text{expression of gene}_i \times \beta_i)$, where β is the regression coefficient.

We divided the GC patients into high-/low-risk groups according to the median risk score. Kaplan–Meier survival curves were then plotted to display the differences in survival, and receiver operating characteristic (ROC) curves at 2, 3 and 4 years were generated to assess the efficiency of the predictive signatures using the timeROC package in the training, test, and entire cohorts.

Validation of the independence and prognostic value of the model in clinical groups

We tested whether the risk score could be an independent prognostic factor excluding the interference of other clinical indicators by integrating corresponding clinicopathological information, including age, sex, grade, and stage, with the risk score to validate the independence of the prognostic model by univariate and multivariate Cox regression analyses. We verified the prognostic value of the risk signature for GC patients by performing a survival analysis of clinical subgroups. Based on the included clinical information, we divided the patients into groups according to an age ≤ 65 years and > 65 years, male and female, G1-2 and G3, and Stage I-II and Stage III-IV. Consistent with the previous calculation method, patients in each group were divided into a high-risk group and a low-risk group by the median value as the boundary, and then Kaplan–Meier curves were generated to evaluate the survival value.

Establishment of a nomogram

The mitochondria-related lncRNA risk score combined with clinicopathological information, including age, sex, grade, stage, T stage, N stage and M stage, was used to construct a nomogram to predict the 2-, 4-, and 6-year survival of GC patients. The predictive capacity of the nomogram was evaluated by calculating the concordance index (C-index) and constructing calibration curves.

Investigation of the immunotherapy response and immune landscape based on the risk signature

The mutation data of GC patients downloaded from TCGA database were analyzed with the R package Maftools [28], the results of which are illustrated in waterfall plots. According to the high- and low-risk groups determined in the training set, we compared the difference in the TMB between the high-risk group and the low-risk group and divided the patients into a high-TMB group and a low-TMB group. A survival analysis was subsequently performed for the TMB level and risk score. We then performed ssGSEA in an attempt to identify immunological reasons for the difference in survival between the high- and low-risk groups. GSEA is a

powerful bioinformatics tool that can clearly show the differences in genes and biological processes between groups [29, 30]. In addition, we further explored the associations between the expression levels of immune checkpoint genes in the two groups.

Functional enrichment analysis of the DEMGs significantly associated with lncRNAs

In addition to focusing on the overall differences between the high- and low-risk groups, we also wanted to determine where specific differentially expressed genes were enriched to better understand the underlying mechanisms. Based on the results presented in the Sankey diagram, DEMGs significantly associated with lncRNAs were identified and subjected to a functional enrichment analysis. Gene Ontology (GO) analysis, including biological processes (BPs), cellular components (CCs), and molecular functions (MFs), was performed to explore the differences in biological functions between the two groups, whereas a Kyoto Encyclopedia of Genes and Genomes (KEGG) analysis was performed to identify and evaluate potential mechanisms and research directions.

Culture and transfection of gastric cells

All gastric cell lines (GES-1, AGS, HGC27, Kato III, SNU-1, OCUM-1, MKN1 and MKN74) were purchased from iCell (iCell Bioscience Inc., Shanghai, China). The cells were cultured in RPMI 1640 medium (Corning, Inc., Tewksbury, MA, USA) supplemented with 10% fetal bovine serum (FBS) (BI, Israel) and a 1% penicillin–streptomycin solution at 37 °C in a humidified cell culture incubator with 5% CO_2. Cell digestion was performed with 0.25% trypsin and 0.02% EDTA for the appropriate time. All the small interfering RNAs (siRNAs) against the target genes and the corresponding negative control (NC) siRNAs were synthesized by RiboBio (Guangzhou, China). Transfections were performed using jetPRIME (Polyplus Transfection, Inc., Illkirch, France) according to the manufacturer's protocol. Briefly, the cells were seeded in six-well plates overnight one day in advance so that the density of the cells reached approximately 30% before transfection. Then, the transfection mixture was incubated at room temperature, added to each well, and the cells were cultured in the appropriate medium for 24 h. After 24 h, the medium was replaced with fresh RPMI1640 medium containing 10% FBS and a 1% penicillin–streptomycin solution. Forty-eight hours after transfection, total RNA was extracted to detect the expression of target genes. The sequences of the AC129507.1 siRNAs used were as follows: siRNA-1 5′-GGCAGATACAACATTTCAA-3′; siRNA-2 5′-CGTAATAAACCTCCACATA-3′; and siRNA-3 5′-CCACTGCATACAAGAGTAA-3′. The sequence of the NC siRNA was as follows: 5′-UUCUCCGAACGUGUCACGUTT-3′.

Quantitative real-time PCR (qRT–PCR)

Total RNA was extracted from cells using a FastPure Cell/Tissue Total RNA Isolation Kit (YiShan Biotech Co., Ltd.). cDNA was synthesized with HiScript II Q RT SuperMix for qPCR (Vazyme Biotech Co., Ltd.). Gene expression was subsequently detected with ChamQ Universal SYBR qPCR Master Mix (Vazyme Biotech Co., Ltd.) on a Bio-Rad CFX96 Real-Time System. The relative mRNA expression was computed by the $2^{-\Delta\Delta Ct}$ method, with GAPDH or β-actin serving as an internal control. The forward and reverse primer sequences for the target genes are listed in Supplementary Table 2.

Western blot

Proteins were extracted from the cells using RIPA lysis buffer (Beyotime Ltd., Shanghai, China) and prepared as 2 mg/ml loading solution with 4X loading buffer (GenScript Tech, Nanjing). After heat denaturation, the same amount of protein was resolved on a 4–20% sodium dodecyl sulfate–polyacrylamide gel electrophoresis (SDS–PAGE) gel and transferred to a PVDF membrane. The PVDF membrane was blocked with 5% skim milk at room temperature for one hour and then cut as needed and incubated with the primary antibody at 4 °C overnight. The next day, after three washes with TBST, the PVDF membrane was incubated with the corresponding secondary antibody at room temperature for 1 h. The PVDF membrane was exposed with the help of ECL reagent to obtain the target protein bands. The primary antibodies used were as follows: GAPDH (1:10,000, rabbit monoclonal antibody; Cell Signaling Technology, USA), GPX4 (1:1000, mouse monoclonal antibody; Proteintech, Wuhan, China), SLC7A11 (1:1000, rabbit polyclonal antibody; Proteintech, Wuhan, China), FTH1 (1:500, mouse monoclonal antibody; Santa Cruz Biotechnology, USA), NRF2 (1:500, mouse monoclonal antibody; Santa Cruz Biotechnology, USA), NCOA4 (1:1000, rabbit monoclonal antibody; Cell Signaling Technology, MA, USA), SOD1 (1:1000, rabbit polyclonal antibody; ABclonal Technology, China), and SOD2 (1:1000, rabbit polyclonal antibody; Proteintech, Wuhan, China).

Cell counting kit-8 assay

After the cells were digested and counted, they were seeded in a 96-well plate at a density of 5000 cells per well, and 6 wells were established for each group. After the cells adhered, the original medium was discarded, and a mixture of CCK8 reagent and medium was prepared at a ratio of 1:10. A total of 110 μl of this mixture was added to each well and incubated for 2 h in a cell

incubator at 37 °C with 5% CO2. Finally, the absorbance (OD value) was measured with a spectrophotometer.

Colony formation assay

After the cells were digested and counted, they were suspended in medium to a density of 1500 cells/ml and seeded in 6-well plates (3000 cells per well) with 3 wells per group. The cells were placed in a constant-temperature incubator for 14 days or observed under a microscope until the number of cells in most single clones was greater than 50 during culture. During this period, the media were changed every 3 days, and cell growth was observed. After cloning, the cells were fixed with 4% formaldehyde and then stained with crystal violet.

Wound-healing assay

Cells in the logarithmic growth phase were digested to prepare a single-cell suspension, and the density was adjusted to $2*10^6$ cells/ml after counting under a microscope. Two milliliters of the single-cell suspension (the total number of cells per well was 2×10^6) was added to each well of a 6-well plate such that the density of the cells in the 6-well plate reached 90–100% after an overnight incubation. The next day, a 10 μl pipette tip was used to create a horizontal wound. Images of the scratch wounds were captured under a microscope at 0 h and 48 h.

Transwell assay

The invasion and migration abilities of the cells were detected by a transwell assay. Cells in the logarithmic growth phase were digested, counted, and adjusted to a density of $1*10^5$ cells/ml (double for the invasion experiment). The transwell chambers were placed in a 24-well plate, 700 μl of medium containing 20% FBS was added to the lower layer of the chamber, whereas 200 μl of serum-free medium containing $2*10^4$ cells was added to the upper layer. After 24–48 h, the cells were fixed with formaldehyde, stained with crystal violet, and then observed and photographed under a microscope.

Stable cell construction

The short hairpin RNA (shRNA) targeting human AC129507.1 (sh-AC129507.1) and nonspecific control shRNA (sh-NC) were synthesized by GenePharma (Shanghai, China). GC cells were seeded in a 6-well plate at a density of $1*10^5$ cells/well, and the lentivirus was then added when the cell confluence reached approximately 30%. After 48–72 h of lentivirus transfection, the cells were selected in the presence of puromycin (5 μg/ml) for one week to generate stable AC129507.1-knockdown cells. The transfection efficiency was verified by qRT–PCR. The sequence of sh-AC129507.1 was as follows: CCACTGCATACAAGAGTAA. The sequence of sh-NC was as follows: 5′- GTTCTCCGAACGTGTCACGT-3′.

Mouse xenograft model

BALB/c-nude mice (female, 4–6 weeks of age, weighing 18–20 g), which were maintained under specific pathogen-free (SPF) conditions, were randomly distributed into the indicated groups (n = 5). The constructed GC cells were injected subcutaneously into the mice ($1*10^7$ AGS cells per 100 μl were subcutaneously injected into one mouse, while $3*10^6$ HGC27 cells per 100 μl were subcutaneously injected into one mouse). The tumor volume was calculated as $(\text{length}\times\text{width}^2)/2$. The tumor size was monitored weekly, and the mice were sacrificed at 5 weeks after transplantation. The dissected tumor xenografts were used to compare the tumor volume and tumor weight of each group. All animal experiments were reviewed and approved by the Experimental Animal Ethics Committee of the First Affiliated Hospital of Zhejiang University.

Malondialdehyde (MDA) detection

The GC cells from each group were collected after being transfected with siRNAs. The proteins were extracted from the cells using RIPA lysis buffer (Beyotime Ltd., Shanghai, China), the protein concentrations were determined using a BCA protein assay kit (Beyotime Ltd., Shanghai, China), and the MDA concentration was subsequently determined using a lipid peroxidation MDA test kit (ABclonal, China). The ratio of the MDA-to-protein concentration was determined by calculating the MDA content.

Intracellular ROS assay

GC cells were inoculated in 6-well plates and transfected with the corresponding siRNA for 2 days, after which a ROS assay kit (S0033, Beyotime, China) was used to detect the intracellular ROS levels. Briefly, the DCFH-DA solution was diluted in serum-free medium at a ratio of 1:1000. The cell culture medium was removed, an appropriate volume of diluted DCFH-DA solution was added, and the mixture was incubated with the cells in a cell incubator at 37 °C for 20 min. The DCFH-DA solution was discarded, and the cells were washed three times with serum-free cell culture medium to fully remove the DCFH-DA that did not enter the GC cells. Then, the appropriate volume of 1X Hoechst 33342 was added, and the cells were incubated at room temperature for 10 min in the dark. After the Hoechst 33342 solution was discarded, the cells in the 6-well plates were washed with PBS three times. After proper air drying, photos were captured under a fluorescence microscope, and the

number of ROS-positive cells was counted. The experiment was repeated three times.

Cellular apoptosis assay

The cellular apoptosis rate was assessed with an Annexin V-FITC/PI Apoptosis Detection Kit (Vazyme Biotech Co., Ltd., China) according to the manufacturer's instructions. Briefly, the GC cells from each group were collected and washed twice with precooled PBS after being transfected with siRNAs. The transfected GC cells were stained with FITC-Annexin V and PI for 30 min at room temperature in the dark. The percentage of apoptotic cells in each group was detected by flow cytometry (BD, USA). The experiments were repeated three times.

Statistical analysis

R software 4.0.5, ImageJ and GraphPad Prism 8 software were used for visualization and statistical analyses. Data were compared between the two groups using unpaired Student's t test, and all experiments were repeated at least three times. All statistical tests with $p < 0.05$ (two-sided) were considered statistically significant.

Results

Identification of the mitochondria-related lncRNA signature for the final model

A total of 16,876 lncRNAs were extracted from the GC cohort in TCGA database. In addition, we screened 704 DEMGs among 1136 mitochondria-related genes by a differential expression analysis. Combining the above information, we identified 1571 mitochondria-related lncRNAs, as shown in the Sankey diagram (Fig. 1A). Moreover, 360 DEMGs that were significantly correlated with mitochondria-related lncRNAs were also identified (Fig. 1A). The final risk model was constructed by randomly assigning 293 GC patients meeting the screening criteria to the training set and the test set at a ratio of 1:1. The chi-square test revealed no significant difference in clinicopathological characteristics between the two groups (Table 1). We further identified 108 prognostic mitochondria-related lncRNAs by the univariate Cox regression analysis (Table 2). LASSO regression was then adopted to filter out the unsuitable mitochondria-related lncRNAs and avoid model overfitting (Fig. 1B, C). Furthermore, a prognostic signature incorporating nine mitochondria-related lncRNAs was built by a multivariate Cox regression analysis (Fig. 1D). In addition,

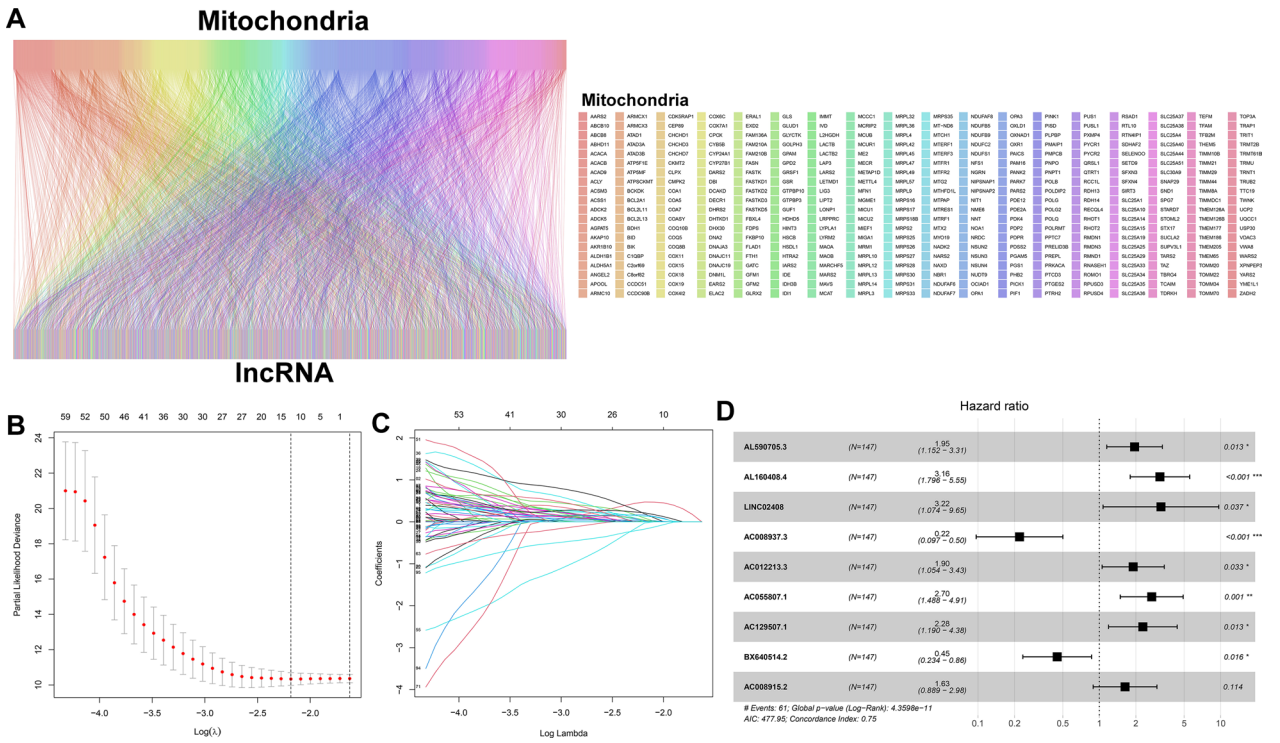

Fig. 1 Identification of the mitochondria-related lncRNA signature included in the final model. **A** Sankey diagram showing the correlations between differentially expressed mitochondria-related genes (DEMGs) and lncRNAs with correlation coefficients > 0.5 and P < 0.001. **B** Dotted vertical lines were drawn at the optimal values using the minimum criteria. **C** LASSO coefficients of the prognostic mitochondria-related lncRNAs. **D** Identification of specific mitochondria-related lncRNAs by a multivariate analysis

Table 1 Clinical characteristics of GC patients in the training cohort and validation cohort

Covariates	No. of patients			*p* value
	Entire cohort	Validation cohort	Training cohort	
Age				
≤ 65 years	134 (45.73%)	64 (43.84%)	70 (47.62%)	0.6316
> 65 years	158 (53.92%)	81 (55.48%)	77 (52.38%)	
Unknown	1 (0.34%)	1 (0.68%)	0 (0%)	
Gender				
Female	108 (36.86%)	61 (41.78%)	47 (31.97%)	0.1055
Male	185 (63.14%)	85 (58.22%)	100 (68.03%)	
Grade				
G1	6 (2.05%)	2 (1.37%)	4 (2.72%)	0.5764
G2	109 (37.2%)	52 (35.62%)	57 (38.78%)	
G3	172 (58.7%)	89 (60.96%)	83 (56.46%)	
Unknown	6 (2.05%)	3 (2.05%)	3 (2.04%)	
Stage				
Stage I	41 (13.99%)	18 (12.33%)	23 (15.65%)	0.6298
Stage II	96 (32.76%)	51 (34.93%)	45 (30.61%)	
Stage III	118 (40.27%)	61 (41.78%)	57 (38.78%)	
Stage IV	26 (8.87%)	11 (7.53%)	15 (10.2%)	
Unknown	12 (4.1%)	5 (3.42%)	7 (4.76%)	
T				
T1	15 (5.12%)	7 (4.79%)	8 (5.44%)	0.6032
T2	67 (22.87%)	31 (21.23%)	36 (24.49%)	
T3	140 (47.78%)	75 (51.37%)	65 (44.22%)	
T4	67 (22.87%)	30 (20.55%)	37 (25.17%)	
Unknown	4 (1.37%)	3 (2.05%)	1 (0.68%)	
M				
M0	268 (91.47%)	138 (94.52%)	130 (88.44%)	0.4065
M1	16 (5.46%)	6 (4.11%)	10 (6.8%)	
Unknown	9 (3.07%)	2 (1.37%)	7 (4.76%)	
N				
N0	86 (29.35%)	40 (27.4%)	46 (31.29%)	0.7436
N1	82 (27.99%)	42 (28.77%)	40 (27.21%)	
N2	61 (20.82%)	34 (23.29%)	27 (18.37%)	
N3	56 (19.11%)	28 (19.18%)	28 (19.05%)	
Unknown	8 (2.73%)	2 (1.37%)	6 (4.08%)	

the relevant results are shown in Supplementary Fig. 1 to clarify the correlations between the 704 DEMGs and nine prognostic lncRNAs.

Establishment of a prognostic risk model based on the nine-lncRNA signature

More precisely, the formula of the nine-lncRNA signature was as follows: risk score = AL590705.3*0.66886188 + AL160408.4*1.149815373 + LINC02408*1.168787096 + AC008937.3*-1.514330673 + AC012213.3*0.64219404 +

Table 2 The prognostic lncRNAs identified by uni-Cox regression analysis

id	HR	HR.95L	HR.95H	pvalue
LINC02526	1.471484	1.030636	2.100903	0.033499
AC026254.2	2.339178	1.235322	4.429414	0.009088
LINC01537	1.842544	1.010671	3.359125	0.046086
AC093642.1	1.869	1.152472	3.031016	0.011237
AC036108.1	1.842273	1.202398	2.822669	0.005006
AC023511.1	1.387128	1.0465	1.838627	0.02284
MYLK-AS2	4.300916	1.396839	13.24267	0.011009
AC087392.2	1.918862	1.239155	2.971402	0.003489
AP001363.2	1.451709	1.030214	2.04565	0.033166
AC011510.1	1.539892	1.077514	2.200683	0.017799
CCAT2	2.355022	1.108568	5.002966	0.025876
AL590705.3	1.916438	1.195711	3.071592	0.00688
AC011997.1	1.818991	1.07058	3.090594	0.026958
MIR1915HG	1.621803	1.117665	2.353338	0.010909
NCKAP5-AS2	2.404346	1.127379	5.127716	0.023194
AL359704.2	1.511896	1.043237	2.191091	0.028994
AL354892.2	1.433997	1.088573	1.88903	0.010362
LINC02757	10.86479	2.575852	45.827	0.001161
NNT-AS1	1.414103	1.017683	1.964941	0.03898
AC022113.1	2.897176	1.121302	7.48561	0.028066
AC126323.3	1.470832	1.003361	2.156099	0.048024
AP000941.1	1.781095	1.054525	3.008273	0.03089
AC002480.1	2.871796	1.843988	4.472486	3.05E-06
OPA1-AS1	1.820203	1.059844	3.126063	0.029962
AF064860.2	2.068777	1.056115	4.052437	0.034081
LINC02185	2.2285	1.196063	4.152135	0.011608
IRAIN	1.456399	1.047081	2.025725	0.025533
AC093849.1	3.132017	1.10891	8.846101	0.031153
AC068790.7	1.679378	1.109139	2.542793	0.014311
AC004947.1	5.056659	1.259663	20.29893	0.022284
AC002480.2	3.706056	1.960026	7.007481	5.57E-05
AC069029.1	1.66978	1.05351	2.646549	0.029125
AC023908.3	2.080131	1.111008	3.894613	0.022083
AP001528.1	1.349041	1.002313	1.815713	0.048245
LINC01579	1.440916	1.035996	2.004098	0.030003
AC135178.2	3.653031	1.19932	11.12684	0.02262
SOCS2-AS1	1.955171	1.174839	3.253801	0.00988
AL390783.1	2.259508	1.057122	4.829507	0.03544
AL160408.4	2.601506	1.595057	4.243004	0.000128
AC093627.5	1.401525	1.005657	1.953221	0.046231
LINC02853	11.4588	1.985868	66.11931	0.006388
AC087521.1	2.139806	1.129192	4.054908	0.019674
AC005165.1	1.474927	1.076891	2.020082	0.015453
AC080129.1	2.34215	1.08041	5.077391	0.031093
AC091614.1	2.568457	1.025608	6.432257	0.044015
LINC02408	5.02061	1.844462	13.66606	0.001587
AL157371.2	2.036215	1.118862	3.705702	0.019934
BAALC-AS1	2.091637	1.149108	3.807253	0.015745
AC097359.2	1.734551	1.050143	2.865007	0.031472

Table 2 (continued)

id	HR	HR.95L	HR.95H	pvalue
ZNF8-ERVK3-1	2.009697	1.034179	3.905398	0.039484
LINC02137	4.363092	1.180354	16.12785	0.027206
TMEM18-DT	15.65138	1.754659	139.6088	0.013756
AC091153.3	1.514632	1.08522	2.113958	0.014656
AC139887.2	1.775686	1.209939	2.605968	0.00335
AC008937.3	0.414488	0.186675	0.920316	0.030465
SERPINB9P1	1.426588	1.060332	1.919354	0.018928
AC025165.5	1.570615	1.097128	2.248445	0.01365
HMGA2-AS1	1.654081	1.153379	2.372147	0.006225
LINC00163	2.217124	1.154053	4.259457	0.016846
CASC15	2.212598	1.172748	4.174461	0.014209
FRMD6-AS2	1.750307	1.081094	2.833773	0.022777
BOLA3-AS1	1.458281	1.106096	1.922603	0.007474
AL121772.1	0.724758	0.529855	0.991354	0.043978
LINC01489	3.562492	1.152736	11.00976	0.027323
C15orf56	1.923966	1.077742	3.43463	0.026886
AL031668.2	1.435887	1.163777	1.771622	0.000739
AC000050.2	1.28175	1.029085	1.596451	0.026699
AL449983.1	2.035803	1.174343	3.529202	0.011326
AC012213.3	2.224992	1.270109	3.897766	0.005177
MYOSLID	3.225392	1.527747	6.809475	0.00213
AC041005.1	8.50882	1.456083	49.72243	0.017448
HGC6.3	1.886665	1.054464	3.375655	0.032466
AC084880.3	2.247277	1.242215	4.065524	0.007427
AC118658.1	1.779381	1.281698	2.470314	0.000576
AC055807.1	2.678343	1.583473	4.530243	0.000239
AC012055.1	2.539589	1.186172	5.437247	0.016416
AC133785.1	2.058642	1.245751	3.401968	0.004842
AL161457.2	3.960316	1.176941	13.32616	0.026208
AC092794.2	1.376623	1.000161	1.894786	0.049884
AC007687.1	1.748318	1.061201	2.880335	0.028296
AC005009.1	2.206641	1.317968	3.694525	0.002613
PKP4-AS1	4.246453	1.464496	12.31301	0.00776
AC005076.1	1.506721	1.041245	2.180282	0.02968
AL157931.1	1.572479	1.022765	2.417653	0.039157
AC048382.5	2.944088	1.054935	8.216291	0.039199
AC129507.1	2.330744	1.352951	4.015201	0.002294
AP002907.1	1.57013	1.001718	2.46108	0.049131
ZNF582-AS1	1.689931	1.099043	2.598501	0.01684
LINC01571	12.11445	2.054079	71.44807	0.005869
AL442125.1	1.788445	1.014581	3.152571	0.04443
AC012409.3	2.096072	1.106052	3.972254	0.023268
AC026691.1	2.212766	1.069393	4.57861	0.03229
AP002761.1	1.616549	1.053238	2.481142	0.028002
DIRC3	3.969894	1.027385	15.33998	0.045594
BX640514.2	0.420303	0.227798	0.775486	0.005544
AC002456.1	8.216092	1.974995	34.17942	0.003783
LNCAROD	1.466454	1.118464	1.922716	0.005606
RDH10-AS1	2.132743	1.047837	4.340934	0.036723

Table 2 (continued)

id	HR	HR.95L	HR.95H	pvalue
AC008915.2	2.312739	1.37835	3.880554	0.001497
AL033519.5	1.522274	1.021086	2.269464	0.039172
AL355516.1	1.442106	1.006704	2.06582	0.04589
BAALC-AS2	2.144749	1.240937	3.706836	0.006272
AL713965.1	2.43533	1.041019	5.697141	0.040104
AL731702.1	2.325004	1.101127	4.909189	0.026926
AC025279.1	2.695173	1.025487	7.083423	0.044324
CHASERR	1.736399	1.134599	2.657399	0.011035
Z97989.1	1.919343	1.147948	3.209099	0.012916
AP001029.1	1.449509	1.027463	2.044915	0.034492

AC055807.1*0.994224804 + AC129507.1*0.825667702 + BX640514.2*-0.799392558 + AC008915.2*0.488035795. The risk scores of the GC patients in the training cohort were calculated, and we split the patients into a high-risk group and a low-risk group bounded by the medium-risk score (Fig. 2A). Kaplan–Meier curves indicated that patients in the high-risk group experienced shorter OS and PFS than patients in the low-risk group (Fig. 2B, C).

Assessment of the risk model

ROC curves were generated to evaluate the predictive ability of the risk model. The area under the curve (AUC) values of the ROC curves for predicting 2-, 3-, and 4-year survival ranged from 0.845 to 0.876 (Fig. 3A), which indicated that the prognostic model had a satisfactory predictive capacity. The AUC of the 3-year survival rate revealed that the risk score (0.876) and age (0.664) had good predictive abilities and that the C-index of the risk score was better than that of the other clinicopathological factors (Fig. 3B, C). Driven by the good predictive power of the prognostic signature, we wanted to test the independence of the risk score. Univariate and multivariate Cox regression analyses were subsequently conducted to validate the independence of the risk score by combining relevant clinicopathological information, such as age, sex, grade, and stage, with the risk score (Fig. 3D, E). The risk score was an independent prognostic factor independent of other clinical factors ($P < 0.05$), which was consistent with the results for age. We further validated the risk model from a clinicopathological perspective to explore the consequences of the risk model. As shown in Fig. 3F–I we observed a statistically significant difference in the prognosis between the groups in terms of age, sex, G3 stage and stage, while no significant difference was observed in the G1-2 group. In summary, our model could also be applied to different clinical parameters.

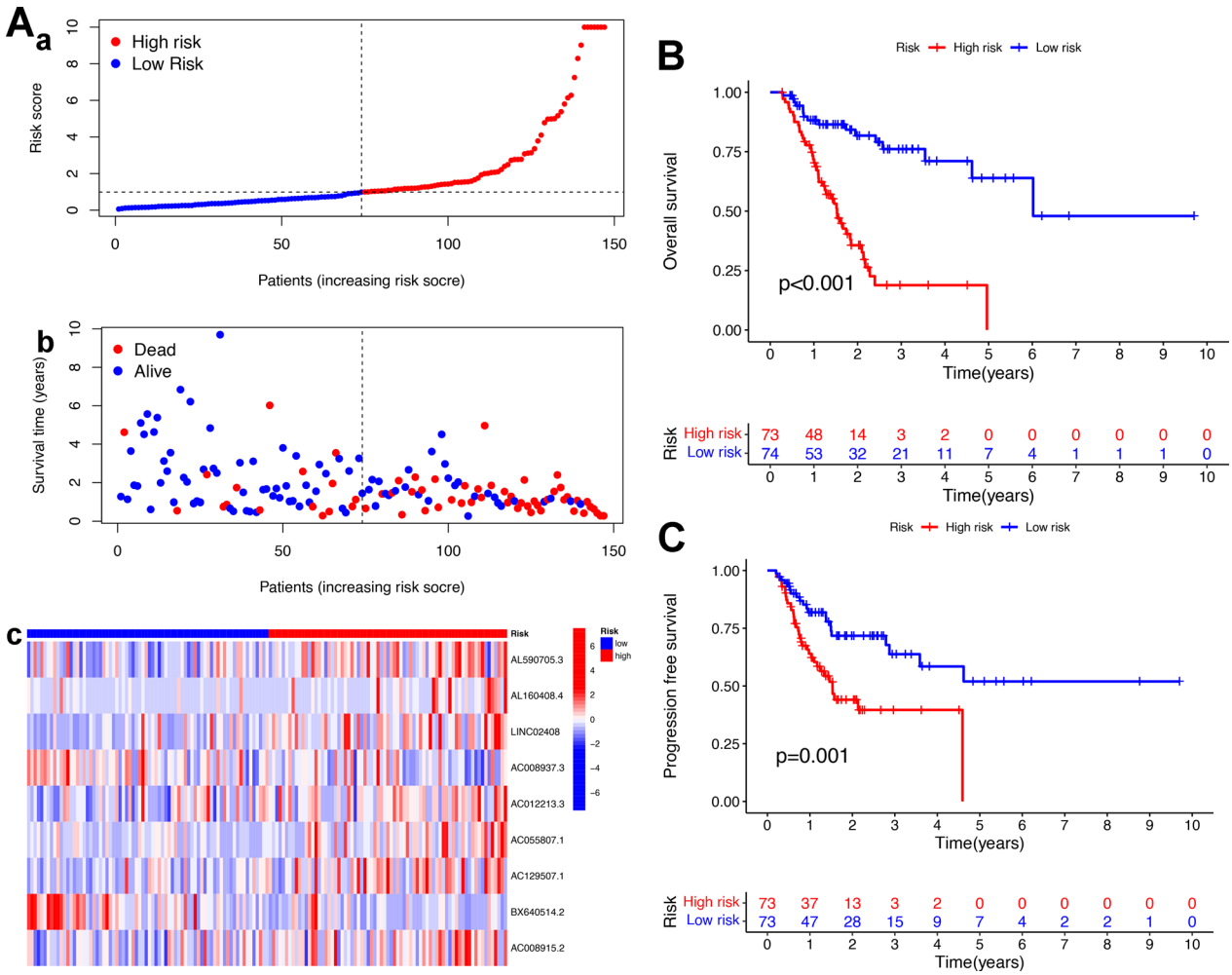

Fig. 2 Construction of the prognostic model based on the nine-lncRNA signature in the training cohort. **A** a. Risk score distribution of patients with GC using the nine-lncRNA signature. b. Scatter plots showing the survival of GC patients. c. Heatmap of the expression of the nine lncRNAs in the high-risk and low-risk groups. **B** Kaplan–Meier survival curves showing the difference in overall survival (OS) between low-risk and high-risk patients. **C** Kaplan–Meier survival curves showing the difference in progression-free survival (PFS) between low-risk and high-risk patients

Validation of the predictive signature

We applied the risk signature to both the training cohort and the entire cohort in the same manner, dividing patients into high- and low-risk groups based on the median risk score, to verify the general applicability of the risk signature (Fig. 4A, B). We found that patients in the high-risk group still experienced shorter OS, whether in the training cohort or in the total cohort, which was consistent with the results for the training cohort (Fig. 4C, D). Notably, their ROC curves also showed good predictive performance, which suggested that the risk signature has powerful predictive performance for the prognosis of patients (Fig. 4E, F).

Construction of the nomogram

As a method to further evaluate the clinical practical value of the risk model, a nomogram combining the risk model and other clinicopathological factors, such as age, sex, grade, T stage, N stage, M stage and stage, was constructed to predict the prognosis and survival of patients at 2, 4 and 6 years (Fig. 5A). Moreover, we observed good agreement between the 2-year, 4-year, and 6-year predicted survival rates and the actual survival rate according to the calibration curve (Fig. 5B). Overall, the prognostic risk model based on the nine-lncRNA signature can accurately predict the prognosis of GC patients and has high clinical practicability.

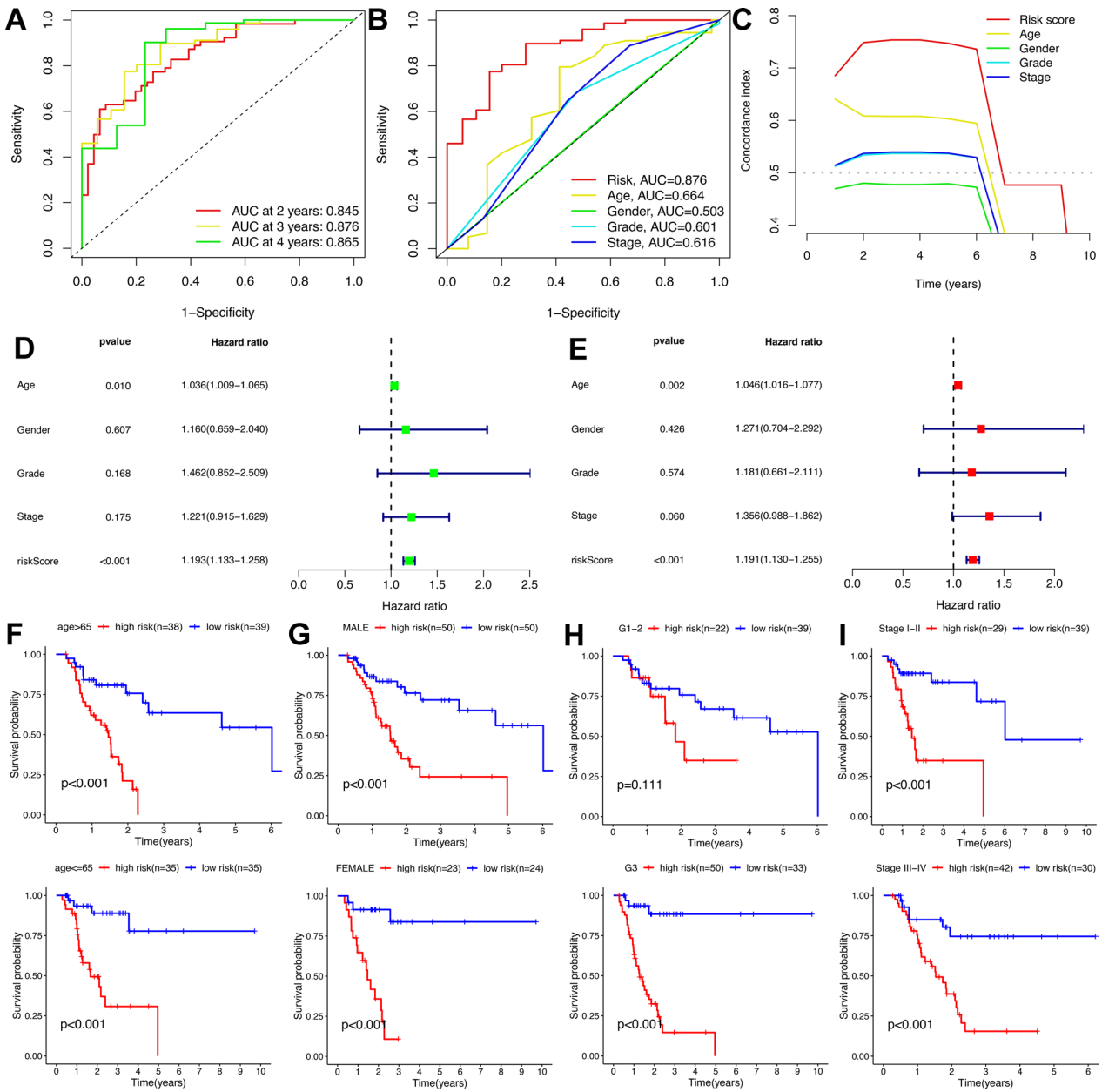

Fig. 3 Assessment of the risk model. **A** ROC curves for the nine-lncRNA signature at 2, 3 and 4 years. **B** ROC curves for the risk score, age, sex, grade and stage. **C** C-indices of the risk score, age, sex, grade and stage. **D** Forest plot of the univariate Cox regression analysis between the risk score and clinicopathological factors. **E** Forest plot of the multivariate Cox regression analysis between the risk score and clinicopathological factors. **F**–**I** The prognostic value of the risk signature stratified by clinicopathological characteristics

Relationship between the TMB status and the risk signature

In recent years, immunotherapy has gradually become a promising approach to improve the prognosis of patients with GC, in which the TMB may be a prognostic factor that cannot be ignored in the response to antitumor immunotherapy [31, 32]. The gene mutation profiles of patients in the high- and low-risk groups are shown in waterfall plots (Fig. 6A, B). According to the waterfall plots, the top five genes with high mutation frequencies in the high-risk group were TTN (43%), TP53 (42%), CSMD3 (22%), MUC16 (21%), and SYNE1 (21%), whereas the top five genes with high mutation frequencies in the low-risk group were TTN (57%), TP53 (43%), MUC16 (36%), LRP1B (34%), and ARID1A (32%). Moreover, we also found that the gene mutation frequencies

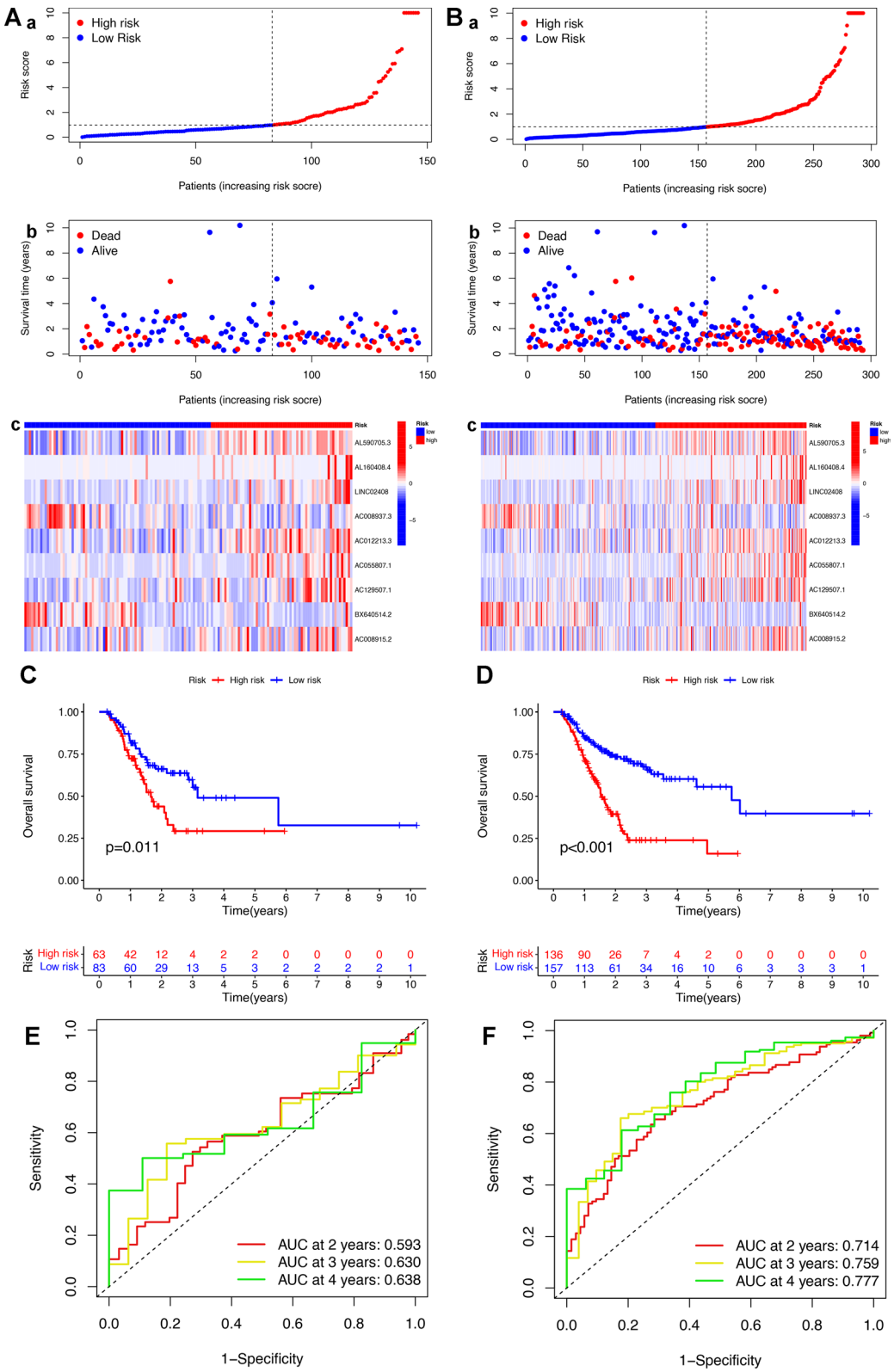

Fig. 4 Internal validation of the predictive signature. **A**, **B** a. Risk score distribution of patients with GC using the nine-lncRNA signature. b. Scatter plots showing the survival of GC patients. c. Heatmap of the expression of the nine lncRNAs in the high-risk and low-risk groups. **C**, **D** Kaplan–Meier survival curves showing the difference in OS between low-risk and high-risk patients. E, F. ROC curves of the nine-lncRNA signature at 2, 3 and 4 years. **A**, **C**, and **E** show the results for the training cohort, and **B**, **D**, and **F** show the results for the total cohort

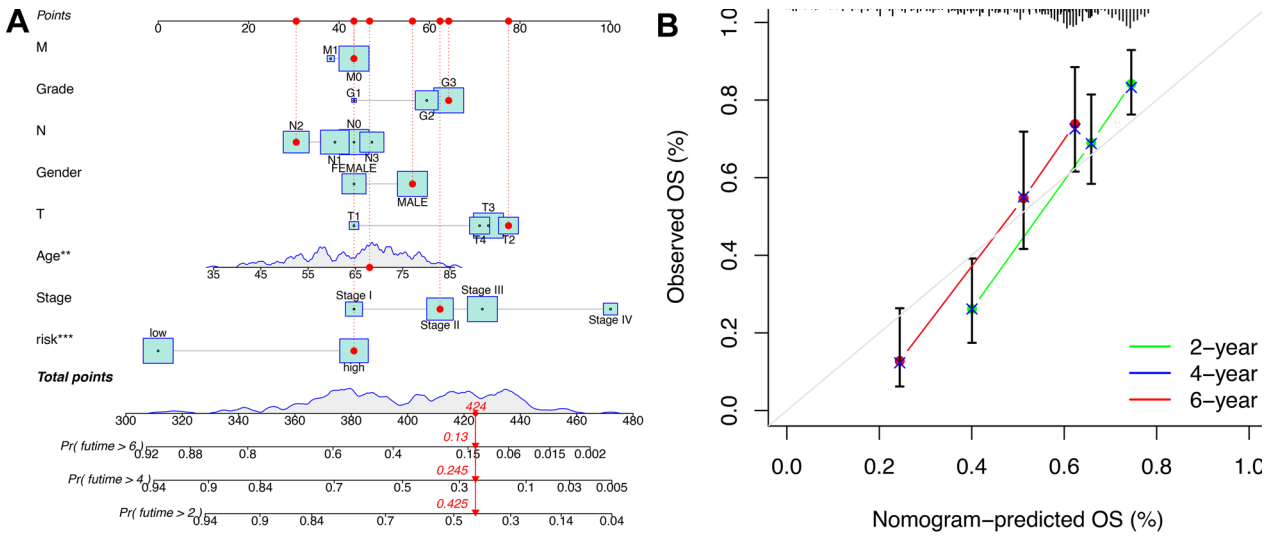

Fig. 5 Establishment of the nomogram for predicting GC patient survival. **A** Nomogram based on risk and clinicopathological factors to predict 2-, 4-, and 6-year survival. **B** Calibration curve between the predicted survival rate and actual survival rate

in the low-risk group were higher than those in the high-risk group, which was consistent with the higher TMB of the low-risk group (Fig. 6C). The survival analysis suggested that patients with a high TMB experienced longer survival than those with a low TMB (Fig. 6D). However, with increasing patient risk scores, the superior survival rate associated with a high TMB status was compromised, which revealed that the combination of the TMB status and the risk signature could predict the prognosis of patients more accurately and scientifically and could guide clinical diagnosis and treatment (Fig. 6E).

Immune cell infiltration landscape and gene enrichment analysis

ssGSEA was adopted to more intuitively determine the interaction between the risk signature and the immune microenvironment in GC patients. We identified significant differences in immune functions, such as chemokine receptor (CCR) expression, antigen-presenting cell (APC) coinduction, checkpoints, T-cell costimulation, cytolytic activity, and MHC class I expression, between the high-risk and low-risk groups, suggesting that the immune function of the low-risk group was more active, consistent with previous conclusions (Fig. 7A). Encouraged by these results, we also further analyzed the differences in immune checkpoints between the two groups. We found that LGALS9 and TNFRSF14 were upregulated in the low-risk group, whereas TNFSF4, TNFSF18, CD200, CD160, CD276, BTNL2 and NRP1 were often upregulated in the high-risk group, reflecting the complexity and variability of the immune microenvironment (Fig. 7B). We next performed GO and KEGG analyses of the differentially expressed genes to determine the underlying mechanism of the differences in survival between the high- and low-risk groups. Intriguingly, in addition to functions related to mitochondria themselves, metabolic functions, such as amino acid activation, cellular respiration and respiratory chain complex assembly, were also enriched in the GO analysis (Fig. 7C). In addition, many metabolic signaling pathways, such as oxidative phosphorylation, fatty acid biosynthesis, arginine and proline metabolism and pyruvate metabolism, were also identified via the KEGG analysis, suggesting that we may be able to interpret the internal mechanism of differences in survival from the perspective of metabolism (Fig. 7D).

Identification of the target lncRNAs from the risk signature

We performed RT–PCR to detect the expression of AC008915.2, AC055807.1, BX640514.2, AL160408.4, AC008937.3, AL590705.3, AC129507.1, LINC02408, and AC012213.3 in GC cell lines (AGS and HGC27) and identify target genes for further research (Fig. 8). The results showed that the expression of each gene was different in the different GC cell lines, among which AC129507.1 was stably and highly expressed in AGS cells and HGC27 cells; thus, it was selected for the next experiment (Fig. 8G).

Effect of AC129507.1 on the proliferation and metastasis of GC cells

Another five different GC cell lines were included for the validation of the expression level of AC129507.1 in GC cells. The results suggested that AC129507.1 expression was increased in different GC cell lines (Fig. 9A). Next,

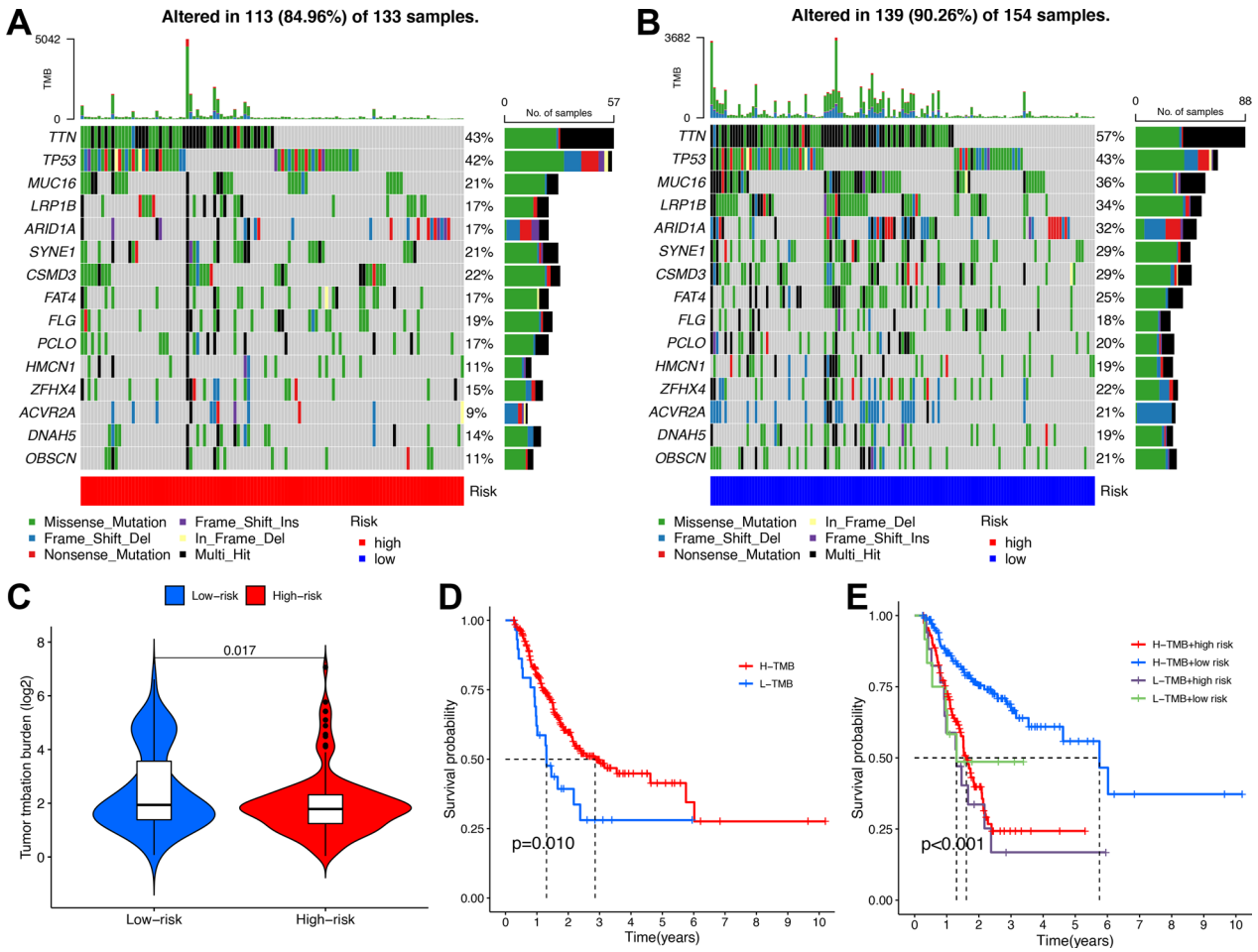

Fig. 6 Analysis of the TMB status of the high- and low-risk groups. **A** Waterfall plot of the gene mutation frequency of patients in the high-risk group. **B** Waterfall plot of the gene mutation frequency of patients in the low-risk group. **C** Analysis of the TMB of the high- and low-risk groups. **D** Survival probability of the high-TMB group and low-TMB group. **E** Survival probability based on an analysis combining the TMB status and the risk score

we analyzed the influence of the AC129507.1 expression level on the prognosis of patients with GC in TCGA database, and the survival analysis revealed that the higher the AC129507.1 expression level was, the worse the prognosis of patients was (Fig. 9B). We further explored the effects of AC129507.1 on the biological behavior of GC cells by constructing three siRNAs targeting AC129507.1 and an NC siRNA and transfected them into AGS cells and HGC27 cells. The RT–PCR results revealed that AC129507.1–1, AC129507.1–2 and AC129507.1–3 reduced the expression of AC129507.1 in the two cell lines, of which AC129507.1–3 had the highest silencing efficiency (Fig. 9C). Therefore, AC129507.1–3 was used in subsequent experiments. The results of the CCK8 and colony formation assays indicated that knocking down AC129507.1 expression significantly inhibited the short-term and long-term proliferation of GC cells (Fig. 9D, E). Furthermore, wound healing and transwell experiments revealed that the invasion and migration abilities of GC cells were weakened when the expression of AC129507.1 was downregulated (Fig. 9F, G). More importantly, subcutaneous xenograft experiments were performed to examine the effect of AC129507.1 on tumorigenicity. We found that the tumors induced by the AC129507.1-silenced cells were significantly smaller than those induced by the control cells, which was accompanied by reductions in the volume and weight of the transplanted tumors (Fig. 9H). Overall, the upregulation of AC129507.1 expression may play a key role in the progression of GC.

Identification of AC129507.1 as a ferroptosis-related target

Inspired by the results of the enrichment analysis (Fig. 7C, D), we speculated that the effect of AC129507.1

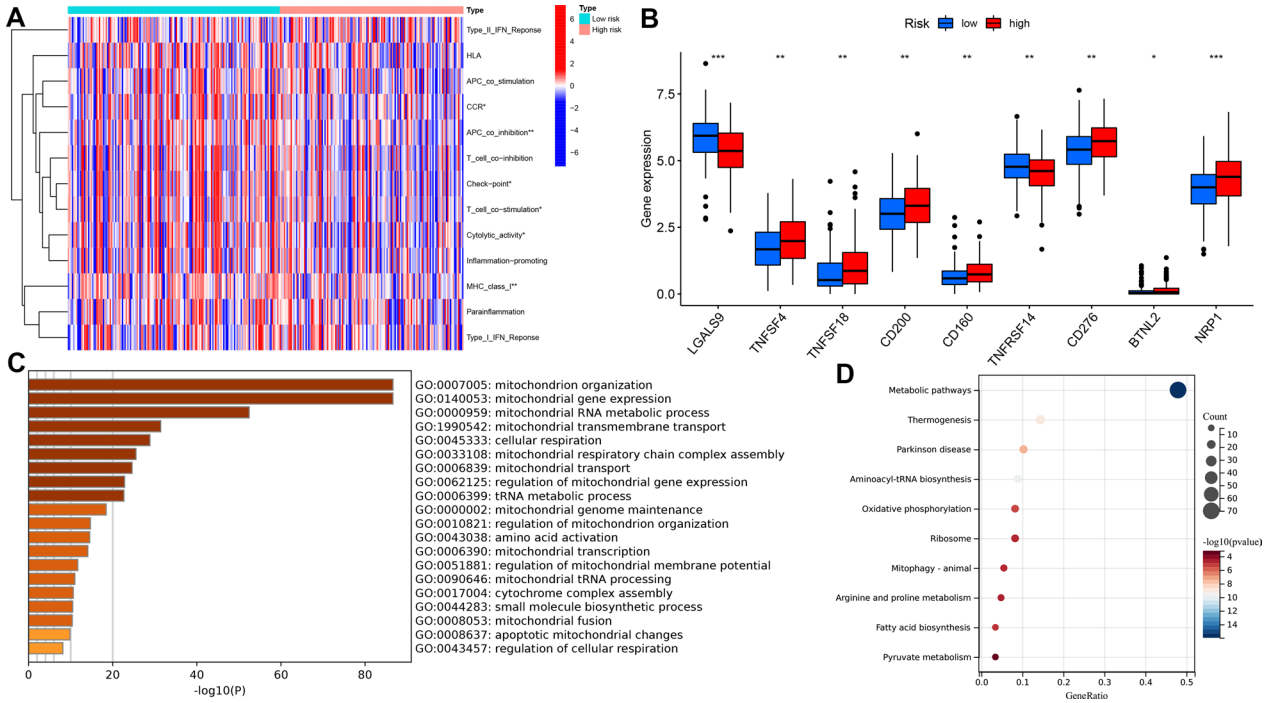

Fig. 7 Immune cell infiltration landscape and gene set enrichment analysis. **A** Differences in immune function between the high- and low-risk groups. **B** Differential expression of immune checkpoint genes between the high- and low-risk groups. **C** GO analysis of DEMGs related to mitochondria-related lncRNAs. **D** KEGG analysis of DEMGs related to mitochondria-related lncRNAs

on the proliferation and invasion of GC cells might be attributed to the inhibition of ferroptosis. Ferroptosis is a mode of cell death induced by the excessive accumulation of iron-dependent lipid peroxides, and the regulatory mechanism involves mainly iron transport, amino acid metabolism and lipid peroxidation, which are closely related to various disease states, such as cancer and neurodegenerative diseases [33–35]. We detected the expression levels of genes related to lipid metabolism in cells after AC129507.1 was knocked down to test this hypothesis, and the results confirmed that the level of intracellular lipid metabolism was significantly increased (Fig. 10A). Moreover, we also examined the mRNA expression of glycolytic enzymes and found that the level of intracellular glycolysis decreased upon AC129507.1 knockdown (Fig. 10B). More importantly, the expression levels of a series of ferroptosis-related genes were further examined. We confirmed that the ferroptosis-related genes GPX4, SLC7A11, FTH1 and NRF2 were significantly downregulated when the expression of AC129507.1 in AGS and HGC27 cells was downregulated, whereas NCOA4 expression exhibited the opposite pattern (Fig. 10C). Since proteins are critical executors of life activities, we subsequently conducted western blotting and found that the changes in the expression of ferroptosis-related proteins were consistent with the PCR results (Fig. 10D). Interestingly, the expression of SOD1, a key factor closely related to cellular oxidative stress, was significantly increased when the expression of AC129507.1 was downregulated (Fig. 10D). Additionally, since lncRNAs are closely related to mitochondria, the localization of the SOD2 protein in the mitochondrial matrix was detected. The results revealed that SOD2 protein expression decreased after AC129507.1 knockdown (Fig. 10D). Next, additional intracellular ROS assays and MDA detection experiments were performed to confirm that the cells underwent ferroptosis (Fig. 10E, F). The results showed that both the intracellular ROS level and the MDA level were increased in AC129507.1-knockdown cells, indicating that the loss of AC129507.1 promotes ferroptosis in GC cells. Since multiple cell death pathways are often activated in the complex tumor microenvironment, we further analyzed the occurrence of apoptosis in these cells using flow cytometry to show that other cell death pathways, such as apoptosis, were not activated in these cells and to reinforce our conclusion. The results revealed that the death mode of these cells was not related to apoptosis (Fig. 10G). Collectively, these results suggested that the downregulation of AC129507.1 promoted ferroptosis, and the changes in intracellular glucose metabolism, lipid metabolism and oxidative stress levels may partially

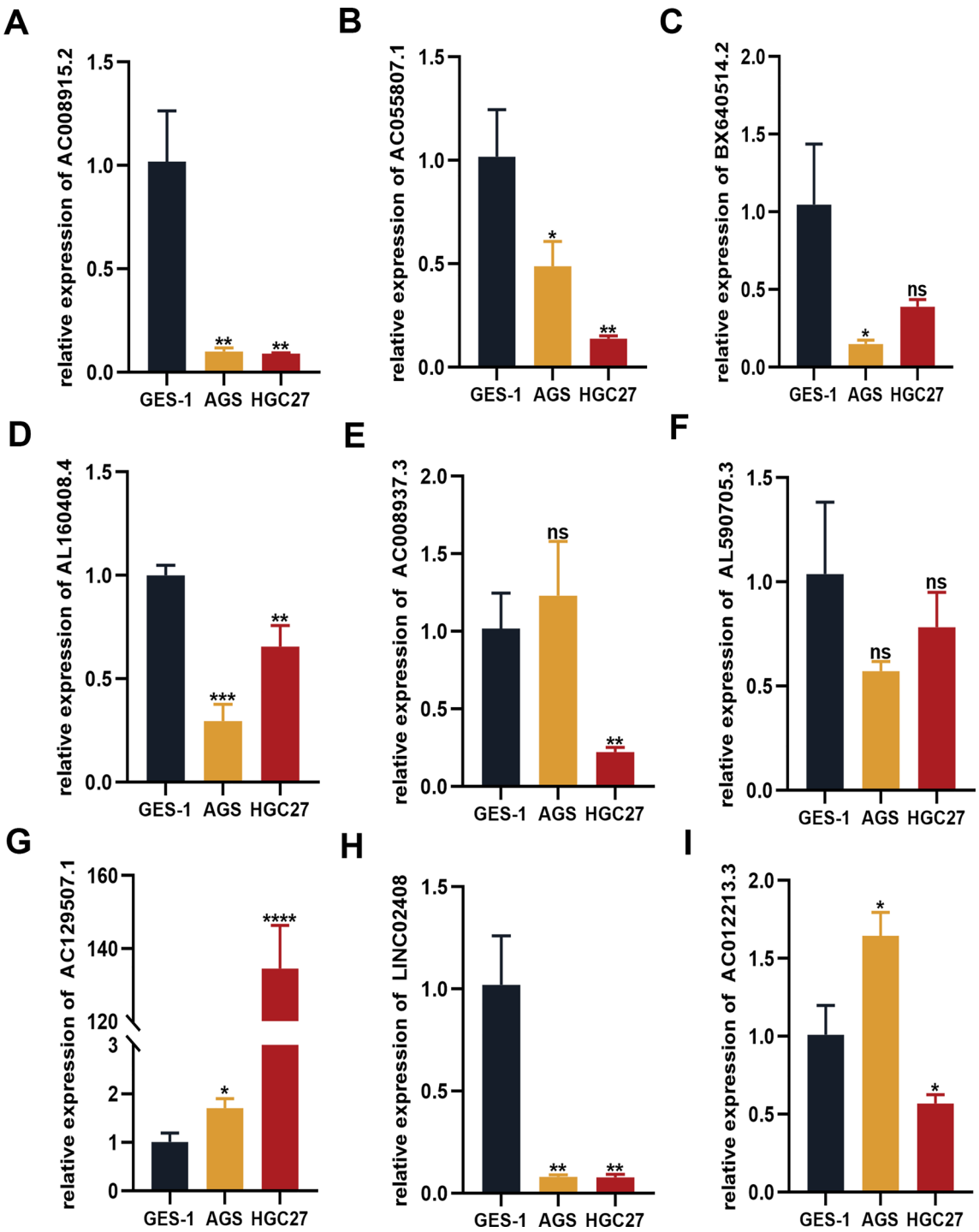

Fig. 8 Identification of the target lncRNAs from the risk signature. RT–qPCR was used to detect the expression of AC008915.2 (**A**), AC055807.1 (**B**), BX640514.2 (**C**), AL160408.4 (**D**), AC008937.3 (**E**), AL590705.3 (**F**), AC129507.1 (**G**), LINC02408 (**H**) and AC012213.3 (**I**) in AGS and HGC27 cells and the results were compared with GES-1 cells. *p < 0.05; **p < 0.01; ***p < 0.001; *ns* not significant

explain the differences in immune cell infiltration in the tumor microenvironment between the high- and low-risk groups.

Discussion

Malignant tumors are a consumptive disease, and metabolic reprogramming is one of their important hallmarks

[36–38]. Briefly, malignant cells often compete fiercely with normal cells for nutrients such as sugars, lipids and amino acids by changing their own metabolism to promote tumor growth and metastasis and eventually gradually hollow out the body. In recent years, research on metabolism and cancer has gradually expanded [38–41]. However, research on the relationships between lncRNAs related to mitochondria, which are energy-generating centers of the body, and cancer is rare, especially in GC. In our study, we collected and integrated the lncRNA data from GC patients in TCGA and intersected them with the mitochondria-related genes obtained by a differential expression analysis to obtain mitochondria-related lncRNAs. We constructed and verified a GC prognostic risk model based on nine lncRNAs through a univariate analysis, LASSO regression, and multivariate analysis. Our risk model not only performed well in predicting the prognosis of patients but also served as a prognostic factor independent of other clinicopathological indicators, demonstrating the potential clinical application value of this risk signature. In addition, the immune infiltration analysis revealed that our risk score was significantly correlated with immune functions in GC, such as CCR, APC coinduction, checkpoints, T-cell costimulation, cytolytic activity, and MHC class I, and the TMB level of the low-risk group was higher than that of the high-risk group, suggesting that the low-risk group had more active immune function, which was consistent with the better survival outcome of the low-risk group.

To the best of our knowledge, our work is the first to focus on the mitochondria-related lncRNAs in GC. The good performance of the risk model prompted us to explore the potential mechanism further. Among the nine-lncRNA signature, we found that only LINC02408, AC012213. 3 and AC129507.1 have been investigated in tumors. First, Daham Kim et al. reported that LINC02408 is highly expressed in thyroid cancer tissues and can be used as a candidate lncRNA to distinguish benign and malignant thyroid nodules [42]. Zhang et al. incorporated LINC02408 into a prognostic model as a competing endogenous RNA and found that this risk model accurately predicted the prognosis of patients with ovarian cancer [43]. Similarly, Luo et al. included LINC02408 in a 5-lncRNA gene signature, which can accurately predict the prognosis of elderly patients with breast cancer and provide clues for clinical decision-making [44]. In addition, Zhong et al. observed that AC012213.3 is highly expressed in breast cancer tissues and cell lines and can promote the growth and metastasis of breast cancer through the RAD54B/PI3K/AKT axis [45]. Research has shown that AC129507.1 not only functions in the construction of a prognostic model as a pyroptosis-related lncRNA to predict the prognosis of prostate cancer patients [46] but also functions in the construction of related prognostic models as a novel cellular senescence-related lncRNA, a differentially expressed lncRNA and a platelet-related RNA to predict the prognosis of GC patients [47–49], which suggests that AC129507.1 is indeed closely related to the occurrence and development of GC and is worthy of further study. Coincidentally, we also found that AC129507.1 was highly expressed in GC cell lines and related to the survival outcomes of GC patients when we screened target genes from GC cell lines based on the nine lncRNAs, which was consistent with the findings of previous studies. The results of the in vitro and in vivo experiments also confirmed that AC129507.1 promoted the proliferation and metastasis of GC cells, suggesting that AC129507.1 may be a potential therapeutic target for GC.

More interestingly, the results of the enrichment analysis of differentially expressed genes revealed a pattern for further research. The enrichment analysis suggested that the differentially expressed genes were enriched in many metabolic functions, such as amino acid activation, cellular respiration, respiratory chain complex assembly, oxidative phosphorylation, fatty acid biosynthesis, arginine and proline metabolism and pyruvate metabolism, suggesting that ferroptosis may be involved in the underlying mechanism. Subsequent basic experiments verified the hypothesis that the knockdown of AC129507.1 expression activated ferroptosis, which manifested mainly as a decrease in ferroptosis-related gene expression, an increase in lipid metabolism levels and a decrease in glucose metabolism levels. Ferroptosis is immunogenic [50, 51], and thus the metabolic upheaval in the tumor microenvironment caused by the occurrence of ferroptosis

(See figure on next page.)

Fig. 9 AC129507.1 is related to a poor prognosis and can promote the proliferation, migration and invasion of gastric cancer cells. **A** AC129507.1 expression in other GC cell lines. **B** Survival curve of AC129507.1 in TCGA GC cohort. **C** The efficiency of AC129507.1 knockdown was verified by RT–PCR. **D**, **E** CCK8 and colony formation assays were performed to compare cell proliferation between the NC group and the AC129507.1-knockdown group. **F**, **G** Wound healing assays and transwell experiments were performed to evaluate the invasion and migration abilities of gastric cancer cells. **H** Results from the subcutaneous xenograft experiments with stable AC129507.1-knockdown GC cells. The left panel shows representative images of dissected xenograft tumors from nude mice in each group, the middle panel shows the tumor volume, and the right panel shows the tumor weight

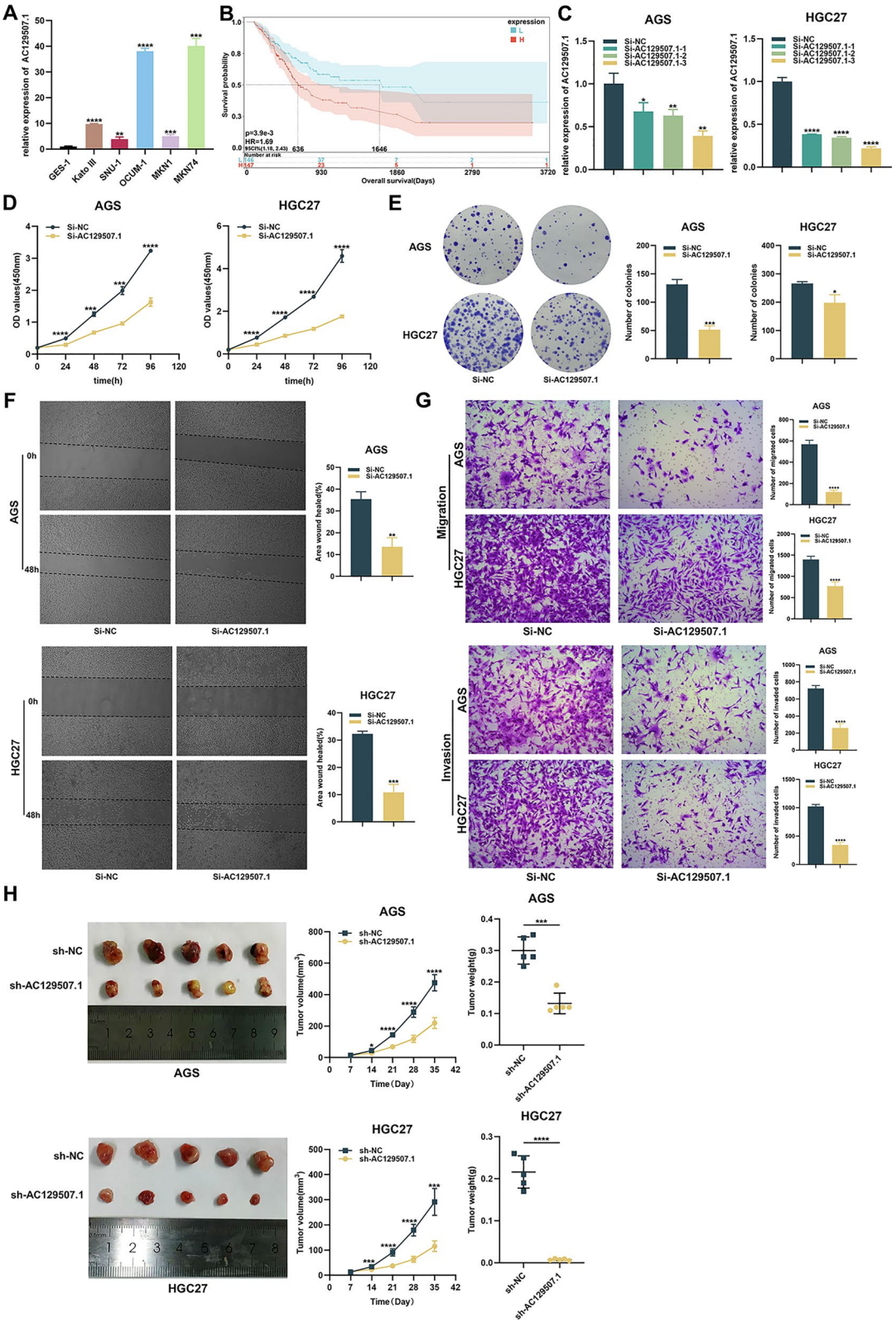

Fig. 9 (See legend on previous page.)

triggers the reorganization of immune cells. Some studies have shown that DAMPs (damage-related molecular patterns) released by cancer cells with ferroptosis can induce the maturation of dendritic cells, cross-induction of CD8 + T cells, the production of IFN-γ and the polarization of macrophages, thus resulting in positive feedback of the immune response, leading to the formation of hot tumors and promoting the occurrence of antitumor immunity, consistent with the results of the immune cell infiltration landscape [52–54]. In addition, glycolysis is downregulated in GC cells when AC129507.1 is silenced, which highlights the famous Warburg effect. The Warburg effect, namely, aerobic glycolysis, is a metabolic feature of almost all cancer cells, resulting in an acidic environment through the excess conversion of glucose into lactic acid, even in the presence of oxygen [55–57]. Studies have shown that the accumulation of lactic acid produced by tumor cells can induce macrophages to develop an inflammatory protumor phenotype, forming a positive feedback loop and accelerating tumor progression and invasion [58, 59]. Therefore, the assumption that the initiation of ferroptosis induced by the silencing of AC129507.1 partially rescued the immunosuppressive microenvironment caused by tumor glycolysis, reshaped the tumor immune microenvironment, and promoted the generation of an antitumor immune response is reasonable. In conclusion, our study elucidated the inextricable relationships between mitochondria-associated lncRNAs and ferroptosis and immunity. However, the underlying mechanism by which AC129507.1 mediates antitumor immunity through ferroptosis at the cellular and molecular levels certainly needs further study.

Another result worth considering is the change in the expression levels of the SOD protein family. Our results indicated that when AC129507.1 was downregulated, increased SOD1 expression and decreased SOD2 protein expression were observed. SOD family members are important antioxidant enzymes that can catalyze the conversion of superoxide radicals into oxygen and hydrogen peroxide, thereby protecting cells from oxidative stress-induced damage [60, 61]. SOD1 is a superoxide dismutase (Cu/ZnSOD) that is present mainly in the cytoplasm of eukaryotic cells, whereas SOD2 is a superoxide dismutase (MnSOD) located in the mitochondrial matrix [60]. Research has shown that ATF3 (activating transcription factor 3) can promote the upregulation of SOD1 expression to induce hydrogen peroxide accumulation, which subsequently promotes iron accumulation and lipid peroxidation triggered by brucine, activating ferroptosis in glioma cells [62]. Moreover, wild-type SOD1 can mutate into pathological H46R and G85R mutant proteins, which can activate ferroptosis and induce familial inherited amyotrophic lateral sclerosis (ALS) [63]. Therefore, considering that SOD1 is located in a complex and variable cytoplasmic environment, we believe that when oxidative stress occurs, although SOD1 expression increases, it may be due to the increased antioxidant capacity of GC cells to cope with intracellular ROS accumulation; on the other hand, the activity and function of SOD1 may be restricted or regulated by other mechanisms, which are worthy of further research. In addition, as a novel mitochondria-related lncRNA, AC129507.1 knockdown induced ferroptosis, resulting in a significant increase in the intracellular ROS level, especially in mitochondria, leading to a decrease in SOD2 expression in mitochondria (64). In summary, we believe that when ferroptosis is initiated, changes in the expression and activity of the SOD protein family, which are the first-line antioxidant system, may be influenced by many factors and require a comprehensive analysis.

Despite these important findings, this study undeniably had some limitations. First, the study lacked external validation because of the absence of GC data from external databases. Second, we preliminarily explored and confirmed the mechanism by which AC129507.1 knockdown induces GC cell apoptosis through ferroptosis, but further exploration of the molecular mechanism and immune-related mechanism is imperative.

Conclusions

In summary, we constructed and validated a nine-lncRNA signature based on mitochondria-related lncRNAs, which showed excellent performance in predicting the prognosis of GC patients. We also analyzed and determined the immunological characteristics of the prognostic model using various bioinformatics tools, providing new insights into the immunotherapy of patients with GC. In addition, through in vitro experiments, we

(See figure on next page.)

Fig. 10 The downregulation of AC129507.1 activates ferroptosis. **A** The expression levels of lipid metabolism-related genes were detected by RT–PCR. **B** The expression levels of glycolysis enzyme-related genes were detected by RT–PCR, and β-actin was used as an internal control. **C** The expression levels of ferroptosis-related genes were detected by RT–PCR. **D** The levels of the GPX4, SLC7A11, FTH1, NRF2, NCOA4, SOD1 and SOD2 proteins were detected using western blotting. GAPDH served as an internal control. **E** Malondialdehyde (MDA) levels were detected after AC129507.1 was knocked down in AGS and HGC27 cells. **F** Intracellular ROS levels were detected in AC129507.1-knockdown GC cells. **G** Apoptosis was detected in AC129507.1-knockdown GC cells by flow cytometry

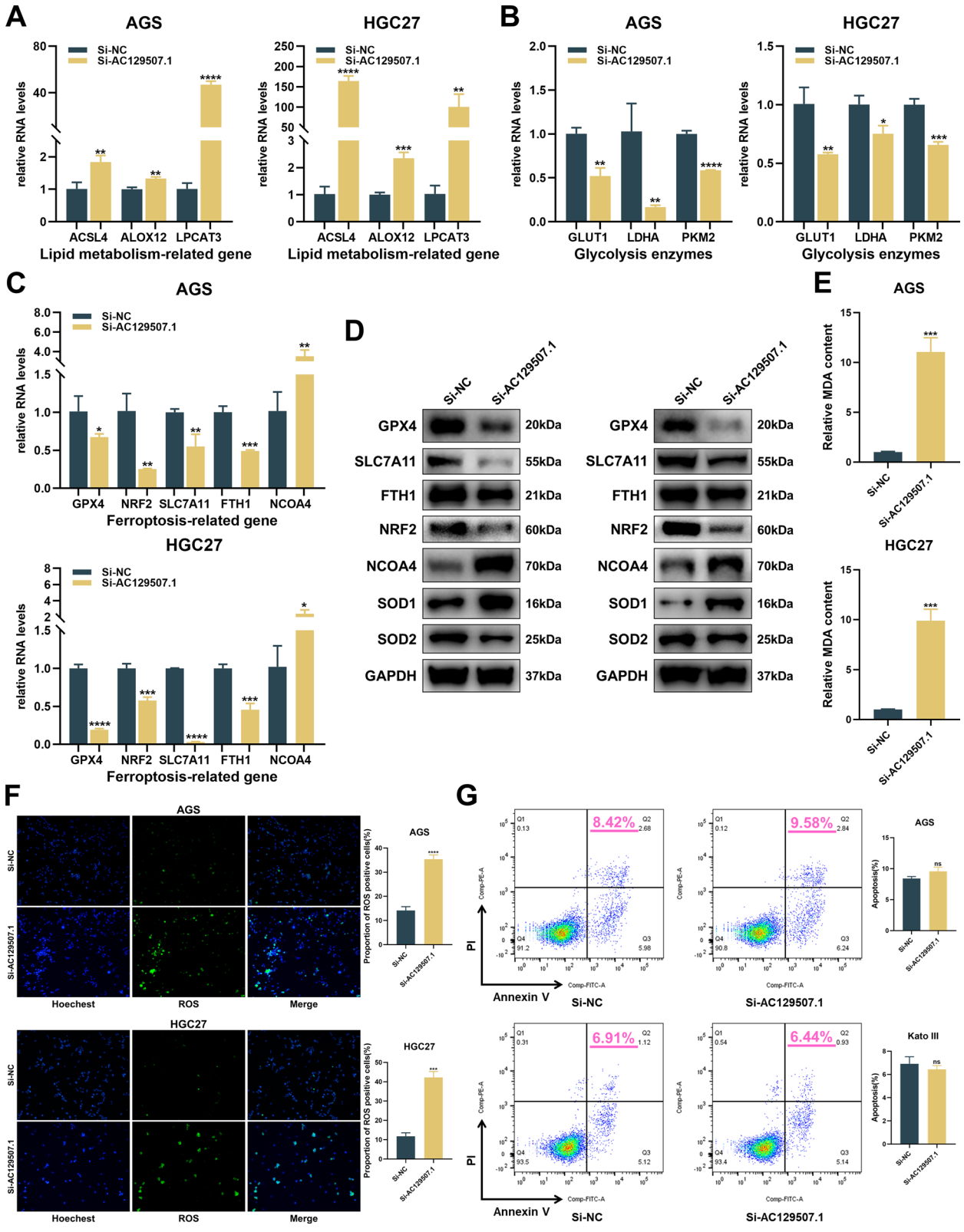

Fig. 10 (See legend on previous page.)

identified AC129507.1 as the target lncRNA and verified that silencing AC129507.1 can inhibit the proliferation, migration and invasion of GC cells by inducing ferroptosis, which may also affect the transformation of the tumor immune microenvironment through changes in glycolipid metabolism and promote the formation of an antitumor immune positive feedback loop.

Abbreviations

GC	Gastric cancer
TCGA	The Cancer Genome Atlas
TMB	Tumor mutation burden
ssGSEA	Single-sample gene set enrichment analysis (ssGSEA)
TCA cycle	The citric acid cycle
ROS	Reactive oxygen species
sunr1	Succinic acid receptor 1
lncRNA	Long noncoding RNA
nt	Nucleotide
DEMGs	Differentially expressed mitochondria-related genes
ROC	Receiver operating characteristic
C-index	Concordance index
GO	Gene Ontology
BP	Biological process
CC	Cellular component
MF	Molecular function (MF)
KEGG	Kyoto Encyclopedia Genes and Genomes
FBS	Fetal bovine serum
siRNA	Small interfering RNA
NC	Negative control
SDS–PAGE	Sodium dodecyl sulfate–polyacrylamide gel electrophoresis
shRNA	Short hairpin RNA
PBS	Phosphate-buffered saline
SPF	Specific pathogen-free
MDA	Malondialdehyde
AUC	Area under the curve
CCR	Chemokine receptor
APC	Antigen-presenting cell
ALS	Amyotrophic lateral sclerosis

Supplementary Information

The online version contains supplementary material available at https://doi.org/10.1186/s12967-025-06287-8.

Supplementary Material 1.

Supplementary Material 2.

Supplementary Material 3.

Acknowledgements
The authors express their gratitude to the public TCGA database for the use of their data.

Author contributions
Donghui Zhou conceived and designed the study with Shanshan Yu. Shanshan Yu drafted the manuscript and analyzed the data with Jinxiao Liang and Lixiao Liu. Ming Chen, Cheng Chen and Shanshan Yu generated the images and the article and reviewed the data. All the authors have read and approved the final published manuscript.

Funding
This project was funded by the National Natural Science Foundation of China (No. 82373246 and No. 82072631).

Availability of data and materials
The datasets used and/or analyzed during the current study are available from the corresponding author upon reasonable request.

Declarations

Consent for publication
All the authors agreed to publish the study.

Competing interests
The authors declare that they have no competing interests.

Author details
[1]Department of Surgical Oncology, The First Affiliated Hospital, School of Medicine, Zhejiang University, Hangzhou 310000, China. [2]Department of Obstetrics and Gynecology, Ningbo City First Hospital, Ningbo University, Ningbo, China. [3]Department of Surgical Oncology, Children's Hospital, Zhejiang University School of Medicine, Hangzhou, China.

Received: 29 August 2024 Accepted: 23 February 2025
Published online: 06 March 2025

References

1. Sung H, Ferlay J, Siegel R, Laversanne M, Soerjomataram I, Jemal A, et al. Global cancer statistics 2020: GLOBOCAN estimates of incidence and mortality worldwide for 36 cancers in 185 countries. CA A Cancer J Clin. 2021;71(3):209–49.
2. Elizabeth CS, Magnus N, Heike IG, et al. Gastric cancer. Lancet. 2020;396(10251):635–48.
3. Huang Z, Wu C, Liu X, Lu S, You L, Guo F, et al. Single-cell and bulk rna sequencing reveal malignant epithelial cell heterogeneity and prognosis signatures in gastric carcinoma. Cells. 2022;11(16):2550.
4. Negoto T, Jo M, Nakayama I, Morioka M, Takeuchi K, Kawachi H, et al. Profiling chromosomal-level variations in gastric malignancies. Cancer Sci. 2022;113(11):3864–76.
5. Anubhav S, Pransu S, Shashank M, Sabiya A, Neeraj R, Swasti T, et al. Lipid metabolism and mitochondria: cross talk in cancer. Curr Drug Targets. 2021;23(6):606–27.
6. Sonia M, Mariasole P, Ilaria G, Paolo P, Carlotta G. Cancer metabolism and mitochondria: finding novel mechanisms to fight tumours. EBioMedicine. 2020;59: 102943.
7. Lourdes S-A, Judit L-P, María Victoria R-P, Marie A-H. Targeting mitochondrial metabolism for precision medicine in cancer. Cell Death Differ. 2022;29(7):1304–17.
8. Bock F, Tait S. Mitochondria as multifaceted regulators of cell death. Nat Rev Mol Cell Biol. 2020;21(2):85–100.
9. Vasan K, Werner M, Chandel N. Mitochondrial metabolism as a target for cancer therapy. Cell Metab. 2020;32(3):341–52.
10. Wang Y, Patti G. The Warburg effect: a signature of mitochondrial overload. Trends Cell Biol. 2023;33(12):1014–20.
11. Schatten H. The impact of mitochondria in ovarian cancer cell metabolism, proliferation, and metastasis. Adv Exp Med Biol. 2024;1452:119–25.
12. Rabe P, Liebing A, Krumbholz P, Kraft R, Stäubert C. Succinate receptor 1 inhibits mitochondrial respiration in cancer cells addicted to glutamine. Cancer Lett. 2022;526:91–102.
13. Qingqing Z, Qing Z, Tao L, Longya L, Fei W, Hong Z, et al. Lactobacillus plantarum-derived indole-3-lactic acid ameliorates colorectal tumorigenesis via epigenetic regulation of CD8 (+) T cell immunity. Cell Metab. 2023;35(6):943-60.e9.
14. Liu W, Wang Y, Bozi L, Fischer P, Jedrychowski M, Xiao H, et al. Lactate regulates cell cycle by remodelling the anaphase promoting complex. Nature. 2023;616(7958):790–7.
15. Zhang Y, Zhai Z, Duan J, Wang X, Zhong J, Wu L, et al. Lactate: The Mediator of Metabolism and Immunosuppression. Front Endocrinol. 2022;13:901495.
16. Ellingford J, Ahn J, Bagnall R, Baralle D, Barton S, Campbell C, et al. Recommendations for clinical interpretation of variants found in non-coding regions of the genome. Genome medicine. 2022;14(1):73.
17. Chen Y, Dawes R, Kim H, Ljungdahl A, Stenton S, Walker S, et al. De novo variants in the RNU4-2 snRNA cause a frequent neurodevelopmental syndrome. Nature. 2024;632(8026):832–40.

18. Sheykhhasan M, Ahmadyousefi Y, Seyedebrahimi R, Tanzadehpanah H, Manoochehri H, Dama P, et al. DLX6-AS1: a putative lncRNA candidate in multiple human cancers. Expert Rev Mol Med. 2021;23: e17.
19. Zhu S, Wang J, Chen D, He Y, Meng N, Chen M, et al. An oncopeptide regulates mA recognition by the mA reader IGF2BP1 and tumorigenesis. Nat Commun. 2020;11(1):1685.
20. Nandwani A, Rathore S, Datta M. LncRNAs in cancer: regulatory and therapeutic implications. Cancer Lett. 2021;501:162–71.
21. Coan M, Haefliger S, Ounzain S, Johnson R. Targeting and engineering long non-coding RNAs for cancer therapy. Nat Rev Genet. 2024;25(8):578–95.
22. Liu C, Shen A, Song J, Cheng L, Zhang M, Wang Y, et al. LncRNA-CCAT5-mediated crosstalk between Wnt/β-Catenin and STAT3 signaling suggests novel therapeutic approaches for metastatic gastric cancer with high Wnt activity. Cancer Commun (London, England). 2024;44(1):76–100.
23. Dandan L, Li S, Xudong Z, Zhen C, Pan H, Congcong H, et al. LncRNA ELF3-AS1 inhibits gastric cancer by forming a negative feedback loop with SNAI2 and regulates ELF3 mRNA stability via interacting with ILF2/ILF3 complex. J Exp Clin Cancer Res. 2022;41(1):332.
24. Ding Y, Gao S, Zheng J, Chen X. Blocking lncRNA-SNHG16 sensitizes gastric cancer cells to 5-Fu through targeting the miR-506–3p-PTBP1-mediated glucose metabolism. Cancer Metab. 2022. https://doi.org/10.1186/s40170-022-00293-w.
25. Li S, Sun J, Ma J, Zhou C, Yang X, Zhang S, et al. LncRNA LENGA acts as a tumor suppressor in gastric cancer through BRD7/TP53 signaling. CMLS. 2022;80(1):5.
26. Rath S, Sharma R, Gupta R, Ast T, Chan C, Durham T, et al. MitoCarta30: an updated mitochondrial proteome now with sub-organelle localization and pathway annotations. Nucleic Acids Res. 2021;49:D1541–7.
27. Muhammad Abu Shadeque M, James A H, Andrea B. LASSO type penalized spline regression for binary data. BMC Med Res Methodol. 2021;21 (1):83.
28. Mayakonda A, Lin D, Assenov Y, Plass C, Koeffler H. Maftools: efficient and comprehensive analysis of somatic variants in cancer. Genome Res. 2018;28(11):1747–56.
29. Biwen W, Frans VDK, Mariah BMJK, Joen L, Leendert WH. Improving gene set enrichment analysis (GSEA) by using regulation directionality. Microbiol Spectr. 2024;12(3):e0345623.
30. Sebastian C, Jörg H. multiGSEA: a GSEA-based pathway enrichment analysis for multi-omics data. BMC Bioinformatics. 2020;21(1):561.
31. Leader A, Grout J, Maier B, Nabet B, Park M, Tabachnikova A, et al. Single-cell analysis of human non-small cell lung cancer lesions refines tumor classification and patient stratification. Cancer Cell. 2021;39(12):1594-609.e12.
32. Mino-Kenudson M, Schalper K, Cooper W, Dacic S, Hirsch F, Jain D, et al. Predictive biomarkers for immunotherapy in lung cancer: perspective from the international association for the study of lung cancer pathology committee. J Thorac Oncol. 2022;17(12):1335–54.
33. Lee J, Nam M, Son H, Hyun K, Jang S, Kim J, et al. Polyunsaturated fatty acid biosynthesis pathway determines ferroptosis sensitivity in gastric cancer. Proc Natl Acad Sci USA. 2020;117(51):32433–42.
34. Liang D, Minikes A, Jiang X. Ferroptosis at the intersection of lipid metabolism and cellular signaling. Mol Cell. 2022;82(12):2215–27.
35. Wang Z, Yuan L, Li W, Li J. Ferroptosis in Parkinson's disease: glia-neuron crosstalk. Trends Mol Med. 2022;28(4):258–69.
36. Faubert B, Solmonson A, DeBerardinis R. Metabolic reprogramming and cancer progression. Science. 2020. https://doi.org/10.1126/science.aaw5473.
37. Seki T, Yang Y, Sun X, Lim S, Xie S, Guo Z, et al. Brown-fat-mediated tumour suppression by cold-altered global metabolism. Nature. 2022;608(7922):421–8.
38. Tan Y, Li J, Zhao G, Huang K, Cardenas H, Wang Y, et al. Metabolic reprogramming from glycolysis to fatty acid uptake and beta-oxidation in platinum-resistant cancer cells. Nat Commun. 2022;13(1):4554.
39. Rossi M, Altea-Manzano P, Demicco M, Doglioni G, Bornes L, Fukano M, et al. PHGDH heterogeneity potentiates cancer cell dissemination and metastasis. Nature. 2022;605(7911):747–53.
40. Wang Y, Stancliffe E, Fowle-Grider R, Wang R, Wang C, Schwaiger-Haber M, et al. Saturation of the mitochondrial NADH shuttles drives aerobic glycolysis in proliferating cells. Mol Cell. 2022;82(17):3270-83.e9.
41. Jing Y, Cai F, Zhang L, Han J, Yang L, Tang F, et al. Epigenetic regulation of the Warburg effect by H2B monoubiquitination. Cell Death Differ. 2020;27(5):1660–76.
42. Kim D, Yu J, Kim J, Hwang Y, Kim J, Ku C, et al. Use of long non-coding RNAs for the molecular diagnosis of papillary thyroid cancer. Front Oncol. 2022;12: 924409.
43. Zhang Y, Zhou H, Zhang M, Xing L, Yang C, Xia B, et al. Integrated analysis of a competing endogenous RNA network reveals an 11-lncRNA prognostic signature in ovarian cancer. Aging. 2020;12(24):25153–71.
44. Luo Y, Zhang Y, Wu Y, Li H, Shen D, Che Y. Development of a novel five-lncRNA prognostic signature for predicting overall survival in elderly patients with breast cancer. J Clin Lab Anal. 2022;36(1): e24172.
45. Zhong H, Zeng G, He L. Overexpression of the lncRNA AC012213.3 promotes proliferation, migration and invasion of breast cancer via RAD54B/PI3K/AKT axis and is associated with worse patient prognosis. Cancer Manag Res. 2021;13:7213–23.
46. Yu J, Tang R, Li J. Identification of pyroptosis-related lncRNA signature and AC005253.1 as a pyroptosis-related oncogene in prostate cancer. Front Oncol. 2022;12:991165.
47. Zeng C, Liu Y, He R, Lu X, Dai Y, Qi G, et al. Identification and validation of a novel cellular senescence-related lncRNA prognostic signature for predicting immunotherapy response in stomach adenocarcinoma. Front Genet. 2022;13: 935056.
48. Zha Z, Zhang P, Li D, Liu G, Lu L. Identification and construction of a long noncoding rna prognostic risk model for stomach adenocarcinoma patients. Dis Markers. 2021;2021:8895723.
49. Yuan M, Jia Y, Xing Y, Wang Y, Liu Y, Liu X, et al. Screening and validation of platelet activation-related lncRNAs as potential biomarkers for prognosis and immunotherapy in gastric cancer patients. Front Genet. 2022;13: 965033.
50. Tang D, Kang R, Berghe T, Vandenabeele P, Kroemer G. The molecular machinery of regulated cell death. Cell Res. 2019;29(5):347–64.
51. Bebber C, Müller F, Prieto Clemente L, Weber J, von Karstedt S. Ferroptosis in cancer cell biology. Cancers. 2020;12(1):164.
52. Zhao L, Zhou X, Xie F, Zhang L, Yan H, Huang J, et al. Ferroptosis in cancer and cancer immunotherapy. Cancer Commun (London, England). 2022;42(2):88–116.
53. Tang R, Xu J, Zhang B, Liu J, Liang C, Hua J, et al. Ferroptosis, necroptosis, and pyroptosis in anticancer immunity. J Hematol Oncol. 2020;13(1):110.
54. Li J, Liu J, Zhou Z, Wu R, Chen X, Yu C, et al. Tumor-specific GPX4 degradation enhances ferroptosis-initiated antitumor immune response in mouse models of pancreatic cancer. Sci Transl Med. 2023;15(720):eadg3049.
55. Jaworska M, Szczudło J, Pietrzyk A, Shah J, Trojan S, Ostrowska B, et al. The Warburg effect: a score for many instruments in the concert of cancer and cancer niche cells. Pharmacol Rep. 2023;75(4):876–90.
56. Peng L, Zhao Y, Tan J, Hou J, Jin X, Liu D, et al. PRMT1 promotes Warburg effect by regulating the PKM2/PKM1 ratio in non-small cell lung cancer. Cell Death Dis. 2024;15(7):504.
57. Li Y, Gruber J, Litzenburger U, Zhou Y, Miao Y, LaGory E, et al. Acetate supplementation restores chromatin accessibility and promotes tumor cell differentiation under hypoxia. Cell Death Dis. 2020;11(2):102.
58. Paolini L, Adam C, Beauvillain C, Preisser L, Blanchard S, Pignon P, et al. Lactic acidosis together with GM-CSF and M-CSF induces human macrophages toward an inflammatory protumor phenotype. Cancer Immunol Res. 2020;8(3):383–95.
59. Yu S, Hu C, Cai L, Du X, Lin F, Yu Q, et al. Seven-gene signature based on glycolysis is closely related to the prognosis and tumor immune infiltration of patients with gastric cancer. Front Oncol. 2020;10:1778.
60. Elis Cristina Araujo E, Rayne Stfhany SM, Aline DAB, José Raphael MN, Luan DHP. SOD1, more than just an antioxidant. Arch Biochem Biophys. 2020;697 :108701.
61. Maria LG, Nagma S, Timothy CK, Edmund CJ, Doris G. SOD1 is essential for oncogene-driven mammary tumor formation but dispensable for normal development and proliferation. Oncogene. 2019;38(29):5751–65.
62. Shan L, Xuan-Zhong W, Chuan H, Lei W, Shi-Peng L, Chong-Cheng W, et al. ATF3 contributes to brucine-triggered glioma cell ferroptosis via promotion of hydrogen peroxide and iron. Acta Pharmacol Sin. 2021;42(10):1690–702.

63. Li-Qiang W, Yeyang M, Mu-Ya Z, Han-Ye Y, Xiang-Ning L, Wencheng X, et al. Amyloid fibril structures and ferroptosis activation induced by ALS-causing SOD1 mutations. Sci Adv. 2024;10(44):eado8499.
64. Chong Z, Jie L, Ketao Z, Huohui O, Ke S, Qingbo L, et al. SHARPIN promotes cell proliferation of cholangiocarcinoma and inhibits ferroptosis via p53/SLC7A11/GPX4 signaling. Cancer Sci. 2022;113(11):3766–75.

Publisher's Note